Thermal conductivity switch: Optimal semiconductor/metal melting transition

Kwangnam Kim and Massoud Kaviany*
Department of Mechanical Engineering, University of Michigan, Ann Arbor, Michigan 48105-2125, USA

(Received 16 June 2016; revised manuscript received 28 August 2016; published 17 October 2016)

Scrutinizing distinct solid/liquid (s/l) and solid/solid (s/s) phase transitions (passive transitions) for large change in bulk (and homogenous) thermal conductivity, we find the s/l semiconductor/metal (S/M) transition produces the largest dimensionless thermal conductivity switch (TCS) figure of merit $Z_{\rm TCS}$ (change in thermal conductivity divided by smaller conductivity). At melting temperature, the solid phonon and liquid molecular thermal conductivities are comparable and generally small, so the TCS requires localized electron solid and delocalized electron liquid states. For cyclic phase reversibility, the congruent phase transition (no change in composition) is as important as the thermal transport. We identify XSb and XAs (X = Al, Cd, Ga, In, Zn) and describe atomic-structural metrics for large $Z_{\rm TCS}$, then show the superiority of S/M phonon- to electron-dominated transport melting transition. We use existing experimental results and theoretical and *ab initio* calculations of the related properties for both phases (including the Kubo-Greenwood and Bridgman formulations of liquid conductivities). The $5p$ orbital of Sb contributes to the semiconductor behavior in the solid-phase band gap and upon disorder and bond-length changes in the liquid phase this changes to metallic, creating the large contrast in thermal conductivity. The charge density distribution, electronic localization function, and electron density of states are used to mark this S/M transition. For optimal TCS, we examine the elemental selection from the transition, basic, and semimetals and semiconductor groups. For CdSb, addition of residual Ag suppresses the bipolar conductivity and its $Z_{\rm TCS}$ is over 7, and for Zn_3Sb_2 it is expected to be over 14, based on the structure and transport properties of the better-known β-Zn_4Sb_3. This is the highest $Z_{\rm TCS}$ identified. In addition to the metallic melting, the high $Z_{\rm TCS}$ is due to the electron-poor nature of II-V semiconductors, leading to the significantly low phonon conductivity.

DOI: 10.1103/PhysRevB.94.155203

I. INTRODUCTION

The thermal conductivity switch (TCS) is the phenomenon of significant change in thermal conductivity at a distinct temperature, under an external field, or by other means. The TCS performance may be assessed by the ratio of this thermal conductivity change to the smaller of the thermal conductivities, i.e., $\Delta k/k_{\rm min} = Z_{\rm TCS}$, which is called the TCS figure of merit here. The Δk mechanisms are classified in detail in Sec. II by thorough examination of the various thermal energy carriers, namely, phonon, electron (and hole), fluid particle and photon, and transitions. The phonon conductivity (k_p) in the solid phase increases as T^3 at low temperatures ($<0.1\,T_{\rm D}$, Debye temperature) due to the increase in specific heat and decreases as T^{-1} at high temperatures, mainly due to dominant phonon-phonon scattering (mostly by the Umklapp processes) [1]. So, k_p becomes rather small near the melting temperature (T_{sl}). After melting, the fluid (liquid or melt) particles replaces the solid phonons with the fluid-particle thermal conductivity k_f, which is lower but generally comparable to k_p at T_{sl}, as the softened lattice turns into random structure of liquid.

The electronic thermal conductivity (k_e) increases from dielectrics to semiconductors to metals and for metals it becomes independent of temperature near T_{sl} [1]; for intrinsic semiconductors it increases with temperature (increase in the conduction electron density $n_{e,c}$) [2] unless the electron mobility μ_e significantly decreases with temperature. The k_e for semiconductors is much smaller than that of metals, through the generally accepted (even for semiconductors) Wiedemann-Franz (W-F) law ($k_e = N_{\rm L} T \sigma_e$, where $N_{\rm L}$ is the Lorenz number and σ_e is the electrical conductivity), which is also applicable to liquids. So, we expect at melting TCS to have a large Δk when this change is dominated by Δk_e (i.e., $\Delta\sigma_e$) in the transition.

There is also thermal conductivity contribution from the bipolar (combined electron-hole) thermal conductivity (k_{e+h}) in the solid semiconductors, through bipolar diffusion of the thermally excited electron-hole pairs [3,4] transporting additional thermal energy [5]. The photon conductivity becomes important at high temperatures and when the photon absorption coefficient is not small, but generally the conduction electrons absorb photons and here we assume the absorption coefficient is large and k_{ph} is negligible. So, the total thermal conductivity in solid is $k(s) = k_p + k_e + k_{e+h}$ and for liquid is $k(l) = k_f + k_e$. Since k_{e+h} is band-gap and temperature dependent, it is negligible at low temperatures and then has an exponential temperature dependence [4,5]. So, $Z_{\rm TCS}$ can be limited through $k_{\rm min} = k(s)$ with non-negligible k_{e+h}.

Here we review and classify the identified and the potential TCS materials and give some example of each. Then we seek optimal (high $Z_{\rm TCS}$) materials, based on the thermal energy transport mechanisms mentioned above, and use *ab initio* calculations and theoretical treatments to predict these transport properties and introduce the some high $Z_{\rm TCS}$ compounds based on melting transition.

*kaviany@umich.edu

II. THERMAL CONDUCTIVITY SWITCHES (TCSs)

The Z_{TCS} combines Δk at a distinct temperature with large contrast before and after transition through the low k_{min}; i.e.,

$$Z_{TCS} = \frac{\Delta k}{k_{min}}, \text{ TCS figure of merit.} \quad (1)$$

The broad classification of the TCSs is shown in Fig. 1, and thermal conductivity changes and Z_{TCS} for some notable materials with different transitions and mechanisms are shown in Fig. 2 at their distinct transition temperatures. Figure 2 gives the change in thermal conductivity (left axis) as well as Z_{TCS} (right axis) and transition temperature (lower axis) for a range of materials. The TCSs are divided into passive or active based on the lack or existence of external forces or actions exerted on materials. For active, a distant force or mechanism causes the thermal conductivity jump. External forces, electric and magnetic fields, and stress can change the thermal conductivity of materials. Change in thermal conductivity has been observed under electric field in the bees wax during its solidifying [6]. The thermal conductivity of $SrTiO_3$ increases by an applied electric field only below 50 K [7], because the transverse optical (TO) phonon mode degenerated with the longitudinal acoustic (LA) phonon mode is shifted upward by the electric field, weakening the TO-LA interaction, thus increasing the thermal conductivity. The orientation of a uniaxially aligned nematic liquid crystal (cyanobiphenyl, 5CB) changes due to an ac electric field [8] and because its thermal conductivity (albeit small) depends on its molecular orientation [9], it can act at TCSs.

The thermal conductivity of Cu wire is affected by magnetic field, with experiment at 4.2 K recording thermal conductivity decrease and in proportionality under such fields (and the W-F law holding) [10]. They also mentioned negligible field effect on resin, because of the phonon transport dominance (insulator). However, Jin *et al.* [11] have shown that phonons are also affected by magnetic field. They measured thermal conductivities of InSb around 3 K–10 K with and without magnetic field (7 T), concluding that the decrease in thermal conductivity (up to 12% at 5.2 K) is due the anharmonicity of the interatomic bonds under magnetic field. They hypothesize that only the Grüneisen parameter is affected by the field (verified by the *ab initio* calculations). Note that the effect disappears above 9 K.

Simulations have revealed that the thermal conductivity of a ferroic-twinned thin film can be controlled reversibly by mechanical stress [12]. The shear deformation induces the vertical (perpendicular to the heat-flow direction) twin boundaries between the fixed two horizontal twin boundaries in the plastic regime and the emerged boundaries hinder the heat flow by acting as phonon barriers, and the density of the boundaries can be controlled by the magnitude and direction of applied field.

The thermal conductivity of boron nanoribbon is changed at room temperature by wetting the interface with variable solutions [13,14]. Yang *et al.* [14] show that the thermal conductivity of double boron nanoribbon prepared with a mixture of reagent alcohol and deionized water increases, while that with isopropyl alcohol remains the same as that of single boron nanoribbon. To enhance the heat transfer in the film boiling regime, where the heat transfer rate is significantly reduced due to the Leidenfrost effect, it is suggested to attract the slightly levitated liquid (conducting) droplet by a concentrated electric in the gap and decreasing the vapor gap thermal resistance [15]. For thermal controller in small satellites, a MicroElectroMechanical System (MEMS) thermal switch radiator is suggested [16] using a suspended thin membrane with a high emittance coating which contacts with the substrate when a sufficient electric field is applied (heat is emitted into space through the membrane while it is on). Also, Jia *et al.* [17,18] suggest microdevices of liquid-solid thermal

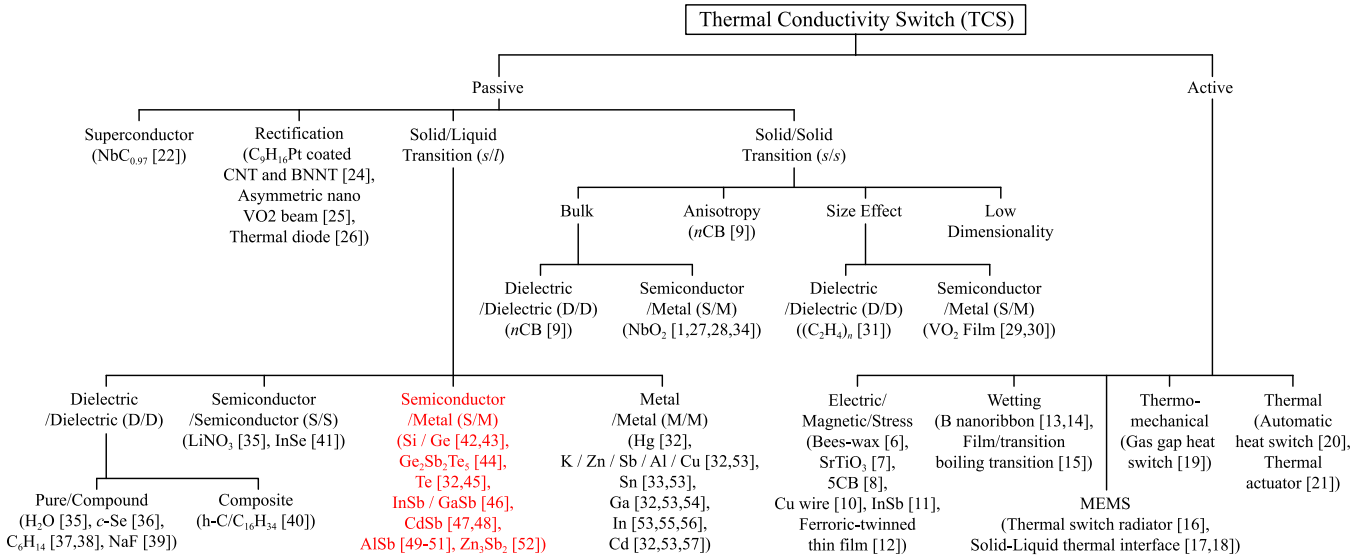

FIG. 1. Classification of thermal conductivity switches (TCSs) with some example materials. The active switches require an external force field or action and are divided based on that mechanism. In passive switches, rectification presents solid-state devices, while others are classified based on the phase transition and the mechanisms of the thermal conductivity jump.

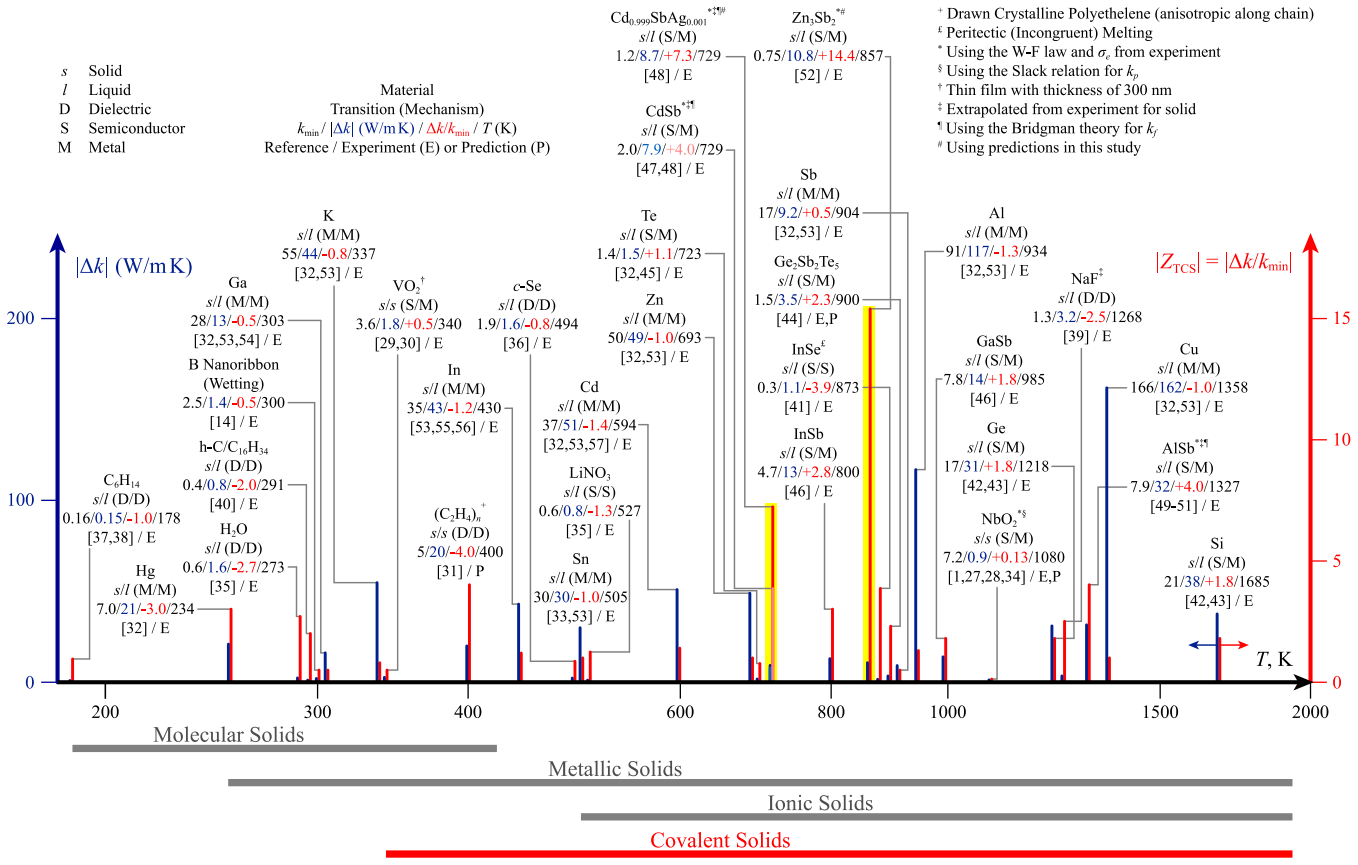

FIG. 2. Thermal conductivity switch (change) $|\Delta k|$ (left axis, blue) and TCS figure of merit $|Z_{TCS}|$ (right axis, red) for some materials at distinct temperatures. The TCS mechanisms and the phase transitions are also shown. D is for dielectric, S is for semiconductor, M is for metal, s is for solid, and l is for liquid. The negative Z_{TCS} indicates the decrease in thermal conductivity upon melting. Two of the highest Z_{TCS} materials, namely, the Ag-added CdSb and Zn_3Sb_2, are marked (yellow). The four bond classifications are also shown.

switch by using liquid body between two plates and liquid initially on the lower plate and controlling the contact with top plate. Their earlier work [17] demonstrates this by an array of discrete liquid droplets which forms a continuous liquid film under mechanical compression between plates, controlling the hydrophilic pattern size and droplet volume. Their later work [18] shows the device with a low-contact pressure switching created through the electroplating, considering the relation between the gap and the capillary force on the separated hydrophobic/philic walls.

There are two thermomechanical switches used in space cryogenic systems: One is a mechanical switch controlled by the contact between surfaces, and the other is the gas-gap heat switch [19] with a movable part. The moving part, controlled by ^{3}He gas with a miniature sorption pump and a permanent neodymium magnet, is the switch (connecting/disconnecting with its counterpart). Another thermal switch for use in cryogenics is the automatic heat switch [20], designed using the pressure dependence of gas thermal conductivity when the gap dimension is smaller than the mean free path of the gas (Knudsen effect). They show that the thermal conductivity increases by a factor of 600 around 15 K–20 K, where the mean free path of nitrogen becomes shorter than the gap (0.5 mm). The gas thermal conductivity becomes independent of the pressure above that temperature. Another thermal/electrical switch uses thermal actuation materials with suitable volume change with temperature (preferably phase change materials) and bridges the gap between the two ends [21].

On the other hand, the thermal conductivities of passive TCS materials change during a transition. Superconductors are passive TCS materials due to their peculiar thermal conductivity behavior. The thermal conductivity of normal materials decreases gradually to zero at 0 K, but that of $NbC_{0.97}$ increases by two orders of magnitude as the temperature decreases below its superconducting transition temperature ($T_c = 10$ K), due to reduction in phonon scattering of the conduction electrons [22]. The reduction can be explained by the Bardeen-Rickayzen-Tewordt (BRT) theory [23] of an ultranarrow electronic band gap developing below T_c, reducing energy states; thus, the probability of phonon-electron scattering decreases and the thermal conductivity increases [22].

The thermal rectification has been widely studied [24–26] and these solid-state devices show the thermal conductivity transition with respect to the heat-flow direction. Carbon nanotubes (CNTs) and boron nitride nanotubes (BNNTs) were engineered to have a nonuniform axial mass by coating with amorphous $C_9H_{16}Pt$, so that they have asymmetric axial thermal conductance at room temperature [24]. The measured thermal conductance was always higher (2% for CNT and 3%–7% for BNNTs) when heat flows from the higher-mass region to the lower-mass region. Similar geometrical treatment

for a VO_2 beam was tested and the nanoscale asymmetric VO_2 beam, which has one narrow end width and the other wider with a uniform thickness, showed that a difference of the thermal conductance with respect to the heat transfer direction of up to 28%, below the transition temperature (340 K), while there is no difference above that temperature [25]. This temperature-gated thermal rectification for the active heat-flow control has been the highest rectification. A macroscopic thermal diode based on switchable thermal clocking can also control the thermal flow [26]. This device, which consists of alternating layers of copper and expanded polystyrene, blocks the heat in one direction whereas it conducts well in the opposite direction; thus, it acts as an electronic diode.

The s/s transitions are accompanied by atomic structure changes; for example, the structure of NbO_2 is changed from a distorted rutile structure under temperature transition (1080 K) to a undistorted rutile structure, and the thermal conductivity increases [27,28]. Also, VO_2 has a monoclinic structure at low temperature under 340 K, while it is tetragonal at higher temperatures [29,30]. During the structural transition of NbO_2 and VO_2, their σ_e increase undergoing semiconductor/metal (S/M) transition, increasing thermal conductivities as shown in Fig. 2. Liquid crystals have directional thermal conductivities and cyanobiphenyl (nCB) has s/s transition temperature (nematic below and isotropic above about 300 K) as the molecular arrangement changes [9]. It was found that the thermal conductivities of samples with a homeotropic orientation decrease at transition during heating, whereas those with a planar orientation increase, for $n = 5$–9 ($|Z_{TCS}| < 0.5$). Also, the highly drawn crystalline $(C_2H_4)_n$ (polyethylene) is predicted (classical molecular dynamics) to decrease distinctly in thermal conductivity at 397 K [31] and is a dielectric/dielectric (D/D) transition.

The s/l phase transition (melting/solidification) can change the thermal conductivity though Δk_e and k_p-k_f due to the absence of distinct lattice in liquid atomic structures (more pronounced than the s/s transitions). Although the k_p and the k_f contribute to the Δk, the Δk_e can be more much effective, so s/l phase transition is classified as D/D, S/S, S/M, and M/M. This is only the electronic mechanism, but it shows the lattice contribution as well as characteristics of each transition. For example, all the TCS with D/D and S/S in Fig. 2 possess negative Z_{TCS}; i.e., $k_p > k_f$ and without the significant increase in σ_e. However, all the S/M TCS (including the s/s transitions, e.g., NbO_2 and VO_2) possess positive Z_{TCS} resulting from the substantial, positive Δk_e, which overcomes $k_p > k_f$, due to the melting into metal. The elemental metals show M/M transition upon melting and have negative Z_{TCS} (expect Bi [33]) because the electron mobility decreases significantly upon melting.

III. HIGH Z_{TCS} WITH SEMICONDUCTOR/METAL (S/M) CONGRUENT MELTING TRANSITION

While large change in the thermal conductivity at a distinct temperature is important, it is also important for the TCS materials to have large contrast in conductivity, i.e., high ratio of thermal conductivity so the heat flux undergoes major change upon transition. So, it is required to have low k_{min}. The s/l TCS should have congruent melting composition to ensure the reversibility for the cyclic melting/solidification. Here, to achieve the highest Z_{TCS}, we consider the passive switch with bulk material (no size effects) and examine each mechanism within this area for the best TCS.

The s/s transitions present a rather small change in the thermal conductivity (small Z_{TCS}), i.e., the increase in k_e due to solid-state atomic structure transition does not notably affect to the thermal conductivity. Also, although the predicted high-draw-ratio crystalline $(C_2H_4)_n$ (polyethylene) shows high Z_{TCS} [31], the conventional polyethylene has a very low thermal conductivity (0.5 W/m K) [58]. Therefore, in general, it appears that the s/s transitions cannot yield high Z_{TCS}, although it should be mentioned that the high Z_{TCS} s/l transitions seem to be limited to high T_{sl}; thus, some materials with these s/s transitions may be attractive.

Among the s/l transitions, the D/D and S/S transitions yield rather small change in thermal conductivity, as shown in Fig. 2. Although some of the examples show relatively large Z_{TCS}, it is due to the rather small k_{min}, so their k ($k_{min} + \Delta k$) does not exceed a few W/mK. The transition temperature depends on the bond type (molecular, ionic, metallic, or covalent), and those are shown below the graph (Fig. 2). The ionic solids which have high T_{sl} lack significant free electrons and so are poor conductors, e.g., NaF with relatively high Z_{TCS} among ionic solids. The molecular solids have strong intramolecular forces and thus are electric insulators, but have low T_{sl} due to weak intermolecular forces. The organic compounds and halogens are examples of molecular solids. The σ_e of ionic solids increases during melting, but is $<10\,(\Omega\,\mathrm{cm})^{-1}$ [39], so k_e gives negligible contribution. The Z_{TCS} of molecular and ionic solids are not high [39,59] and are generally negative, as mentioned before.

From the kinetic theory, for molecular solids with a D/D mechanism (negligible k_e contribution), the ratio of the k_p to k_f at T_{sl} can be approximated as the ratio of the speed of sound in solid and liquid, considering that their the density, specific heat, and mean free path remain the same [59],

$$\frac{k_p}{k_f} \approx \frac{\omega_p}{\omega_f} \approx \frac{1}{\Delta\Omega^{1/3}} \exp\left(\frac{\Delta S_m}{3k_B}\right), \tag{2}$$

where $\omega = u/d$ (u is the mechanical wave speed and d is the mean atomic space), Ω is ordering factor to show the difference in the degree of ordering between phases, S_m is entropy of melting, and k_B is the Boltzmann constant. So, Z_{TCS} for molecular solids is related to ratio of the speed of sound in solid and in liquid at T_{sl}.

InSe has the highest Z_{TCS} among the D/D and S/S transitions, i.e., 3.9. This is due to change between k_p and k_f, because the σ_e is low [60] and continuous across T_{sl} [61]. Its solid σ_e increases with temperature and then decreases from 823 K up to the T_{sl} (873 K). The phase diagram of the In-Se system [62] and the measured properties [63] show that a peritectic melting temperature (incongruent; a different solid phase occurs) of In_4Se_3 marks this transition (823 K). Also, InSe undergoes a peritectic melting at 873 K and passes the liquidus curve near 900 K (the melting and liquidus points may vary) [62–64]. Therefore, InSe is not a good TCS material due to its irreversibility (noncyclic) during the melting and solidifying.

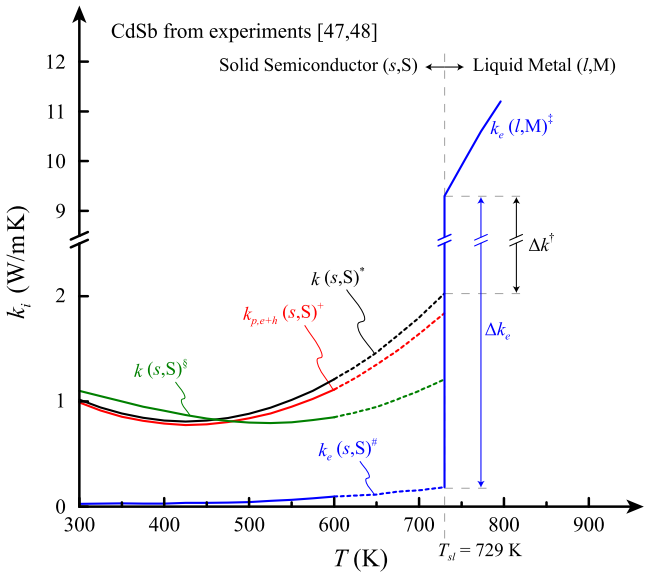

* Experimental result, calculated by measured properties ($k = \alpha\rho C_p$) up to 600 K [48], and extrapolated up to T_{sl}
# Calculated by W-F law using measured electrical conductivity [48], and extrapolated up to T_{sl}
+ $k_{p,e+h}(s,S) = k(s,S) - k_e(s,S)$ [48], the sum of k_p and k_{e+h}
‡ By using measured electrical conductivity [47], k_e is Calculated by W-F law
† Actual Δk will be higher when the fluid particle thermal conductivity is also considered
§ Experimental result for 0.1% Ag added CdSb [48]

FIG. 3. Measured thermal conductivities of pure CdSb as a function of temperature. The semiconductor/metal transition at T_{sl} causes a large increase in electronic thermal conductivity. Addition of 0.1% Ag to CdSb in the solid phase lowers the total thermal conductivity (by 0.8 W/m K at T_{sl}).

The s/l and M/M transition materials (elemental metals) show the highest thermal conductivity change, due to the large change in the σ_e upon melting. For example, the highest $|\Delta k|$ among the elements listed in Fig. 2 is 162 W/m K for Cu. The element with the highest $Z_{\rm TCS}$ is Hg (3.0) at low temperatures. However, other than Hg, the $|Z_{\rm TCS}| < 1.4$ (Cd) [32,53,57], which is lower than elemental semiconductors (1.8 for Si and Ge), because the liquid σ_e is still large (large $k_{\rm min}$). On the other hand, the S/M transition can have higher $Z_{\rm TCS}$ than any other TCS of material with significant Δk upon melting (small σ_e of a solid semiconductor and high σ_e of a metallic liquid).

The epitome of these materials is cadmium antimonide (CdSb), as shown in Fig. 3 (reproduced) [47,48]. It melts congruently at 729 K [62]. The $k(s)$ of CdSb is 2.0 W/m K and the liquid k_e is 9.4 W/m K (at T_{sl} for both); i.e., $Z_{\rm TCS} = 3.7$ (higher when adding k_f), a fairly high value for bulk material without small thermal conductivity in both solid or liquid phases. The large change in the thermal conductivity upon melting is due to the S/M transition, i.e., large Δk_e ($\Delta\sigma_e$) (Fig. 3). The solid thermal conductivity increasing at 425 K, due to the k_{e+h}, which becomes noticeable near 400 K [48]. The $Z_{\rm TCS}$ is further increased when the k_{e+h} is suppressed without decreasing the liquid σ_e. This was done with adding Ag atoms (0.1%), which suppressed the k_{e+h} of CdSb [48] (green curve in Fig. 3). The results show that the thermal conductivity is slightly larger than that without Ag at room temperature [48] (due to the increased $n_{e,c}$, so σ_e), but much lower at high temperatures (1.2 W/m K at T_{sl}), because k_{e+h} is suppressed effectively. However, the effect of the Ag addition on the liquid σ_e will be examined in Sec. VI. Then $Z_{\rm TCS}$ will be around 6.8 (higher when adding k_f).

IV. ATOMIC-STRUCTURE METRICS OF S/M TCS

The phonon conductivity has a strong quadratic dependence on the molar composition [65], but alloying drastically changes in the electronic properties and melting further changes those; e.g., CdSb, a high $Z_{\rm TCS}$ semiconductor compound of metallic Cd and semimetal Sb, has a much lower thermal conductivity than its elements. It can be expected that the thermal conductivity is correlated with several properties which are also related to each other; thus, it is important to understand and find the relations of thermal conductivity and fundamental properties. Figure 4 renders such metrics of high $Z_{\rm TCS}$. For semiconductors the charge effective mass $m_{i,\rm e}$ ($i = e$ or h: electron or hole) is proportional to the band gap ($\Delta E_{e,g}$) and the alloy composition, the static dielectric constant ($\varepsilon_{e,o}$) decreases linearly with $\Delta E_{e,g}$, and $\Delta E_{e,g}(T)$ is linear ($T > 150$ K) with generally negative slope [65]. The effective mass influence the intrinsic charge carrier density ($n_i \propto m_{i,\rm e}^{3/2}$) and mobility ($\mu_i \propto m_{i,\rm e}^{-1}$) [2].

A low $T_{\rm D}$ is preferred for TCS (low phonon conductivity), but the covalent bond needed for solid semiconductor means high T_{sl}, which is proportional to the square of $T_{\rm D}$ ($T_{sl} = C\langle M\rangle T_{\rm D}^2 d^2$, the Lindemann relation [66] for melting, where $\langle M\rangle$ is the average atomic mass, $d^3 = V_a$ is average volume per atom, and C is a constant) [67]. The strong bond leads to the high T_{sl} [67] and large $\Delta E_{e,g}$ [68]. In the report [68], 18 III-V and II-VI compounds show that increase in the atomic number decreases T_{sl} and $\Delta E_{e,g}$ due to expansion of the overlapped atomic potentials leading to the close coupling of the atoms (also, the higher is T_{sl}, the larger is $\Delta E_{e,g}$).

Low $k(s)$ leads to high $Z_{\rm TCS}$, and k_p increases with T_{sl} and decreases with increase in atomic-mass ratio of the constituents [69]. So, compounds with moderate and heavy elements result in high $Z_{\rm TCS}$. While large $\Delta E_{e,g}$ gives small intrinsic k_e, moderate $\Delta E_{e,g}$ is sought to avoid high T_{sl}. CdSb has $\Delta E_{e,g}$ of 0.5 eV. However, the moderate $\Delta E_{e,g}$ can result in significant k_{e+h} at high temperatures. So, intervention is needed to suppress k_{e+h}. Although large $\Delta E_{e,g}$ can give high $Z_{\rm TCS}$, but larger than 4.0 (AlSb in Fig. 5) may not be possible due to very large k_p.

The simple estimation of the k_{e+h} is [70]

$$k_{e+h} = A\exp\left(\frac{-E_{e,g}^*}{2k_{\rm B}T}\right), \tag{3}$$

where A is a constant and $E_{e,g}^*$ is the band gap for the bipolar diffusion. The relation shows that the k_{e+h} will not be negligible if the temperature is sufficiently high, so the k_{e+h} can be suppressed by increasing the band gap [4,5]. However, this increases T_{sl} and $T_{\rm D}$, increasing solid thermal conductivity. Rather, it is preferred for $\Delta E_{e,g}$ to have a weak dependence on temperature (unlike CdSb) so that k_{e+h} can be less effective (less thermal excitation of electrons) at high temperature, but having the S/M transition upon melting. Also, k_{e+h} can be suppressed with the size effect [71]; the nano-PbS suppresses the k_e and k_{e+h} due to the electron scattering at high-density grain boundaries [72], but here

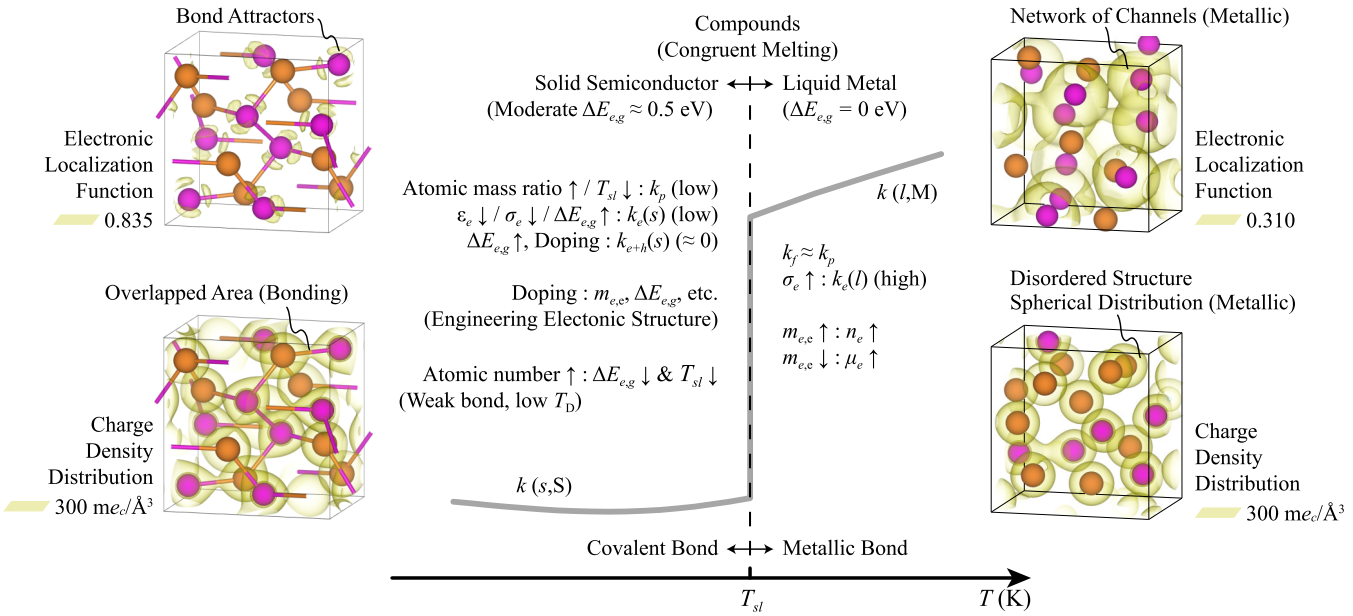

FIG. 4. The optimal S/M melting transition TCS requirements including thermal conductivity for solid and liquid phases. The covalent bonds in solid phase and metallic in liquid phase allow for the electron local-/delocalization, as shown in the ELF and charge density distributions.

we remain with bulk homogeneous materials. In addition to the CdSb, small addition of Ag to PbSe reduces k_p by the point-defect scattering and electron-phonon coupling and k_{e+h} by increasing the hole (majority) density, leading to a decrease in the Seebeck coefficient [48,73]. This can be interpreted with the fact that the k_{e+h} is maximized when the σ_i contributions from electrons and holes are equal [3]; thus, the unbalancing σ_i can reduce the k_{e+h}. Though, suppressing of k_{e+h} is effective with minority-carrier manipulation [74]; decrease in $m_{i,\mathrm{e}}$ (by doping) and μ_i (by microstructure refinement or interface modification) of minority carriers reduces it [5]. These show that k_{e+h} is minimized when the minority carriers are hindered from participating in conduction [75]. In the report [75], band engineering with heterostructure barriers is suggested as a barrier for minority carriers, while the effect on majority carriers is negligible. So, doping for the unbalance by decreasing $m_{i,\mathrm{e}}$, μ_i, and $n_{i,c}$ of the minority carrier and lowering the temperature dependence of $\Delta E_{e,g}$ is effective in suppressing the k_{e+h}, with the additional advantage to reducing k_p by the point-defect scattering.

The large change in σ_e at T_{sl} occurs when solid semiconductors makes a metal transition upon melting. This electron delocalization has history back in Wigner in 1938 suggesting that a free-electron gas should crystalize at low densities (localized in a nonconducting state), and Mott in 1949 discussed this transition (so-called Mott transition) with a crystalline array of monovalent atoms such that the array must be an insulator for large values of lattice parameter and a metal when it reaches a critical value [76]. According to the Mott transition [76], the transition must be discontinuous because electron-hole pair can form because of their Coulomb attraction, $-e_c^2/\varepsilon_e r_{eh}$, where ε_e is the background dielectric constant and r_{eh} is distance, and the binding energy of order $m_e e_c^4/\hbar^2\varepsilon_e^2$, where m_e is the electron mass and $\hbar$ is the reduced Planck constant. The transition occurs when $n_{e,c}^{1/3} R_{\mathrm{B}} \approx 0.2$, where $R_{\mathrm{B}} = 0.53\varepsilon_e/(m_{e,\mathrm{e}}/m_e)$ is the Bohr radius. It shows that the transition occurs when the $n_{e,c}$ and ε_e is large or the $m_{e,\mathrm{e}}$ is small. However, large solid $n_{e,c}$ (large k_e) is not desired, and the $m_{i,\mathrm{e}}$ should be tuned so that both k_e and k_{e+h} are reduced. So, ε_e is key in the binding of the electron-hole and is worth examining near the transition [77].

Although Mott mentioned that the transition is not always discontinuous [76], Mott and Davis [76,78] argued that the transition of semiconductors is a Mott transition, taking account of the disorder of a random array of atoms and ε_e tending to infinity at transition. From Adachi [65], the ε_e semiconductors increases as $\Delta E_{e,g}$ decreases, then ε_e of CdSb will increase with temperature [79] and tends to infinity as $\Delta E_{e,g}$ vanishes upon melting, leading to significant dielectric screening of the Coulomb attraction of the electron-hole pair. Also, the transition should be discontinuous, because solid $\Delta E_{e,g}$, which is about 0.2 eV at T_{sl} for CdSb, suddenly disappears (metallic liquid). Therefore, the CdSb undergoes the Mott transition upon melting, and this is expected for other S/M transition TCS materials.

The other theory describing the criteria for the insulator-metal transition of many liquid alloys is the Ioffe-Regel limit. The scattering of electrons becomes weak due to the screening of the ionic potentials when the $n_{e,c}$ is sufficiently large [nearly free-electron (NFE) metals], and there is a limit where the scattering becomes strong [80]. The electrical conductivity limit (σ_{limit}) at this point is about $3000\,(\Omega\,\mathrm{cm})^{-1}$ for typical liquids and the σ_e follows $\sigma_{\mathrm{limit}}/\eta$, where η is the Korringa enhancement ($\eta > 1$) under the Ioffe-Regel limit ($\sigma_e < \sigma_{\mathrm{limit}}$), where the transport becomes diffusive. Therefore, the σ_{limit} can be considered as the metallic liquid regime for the S/M transition, and favorable TCS materials will have the σ_e higher than σ_{limit}. It should be noted that this theory may not sufficiently consider the remaining short-range order clusters in the metallic liquid; it is expected from this theory that the

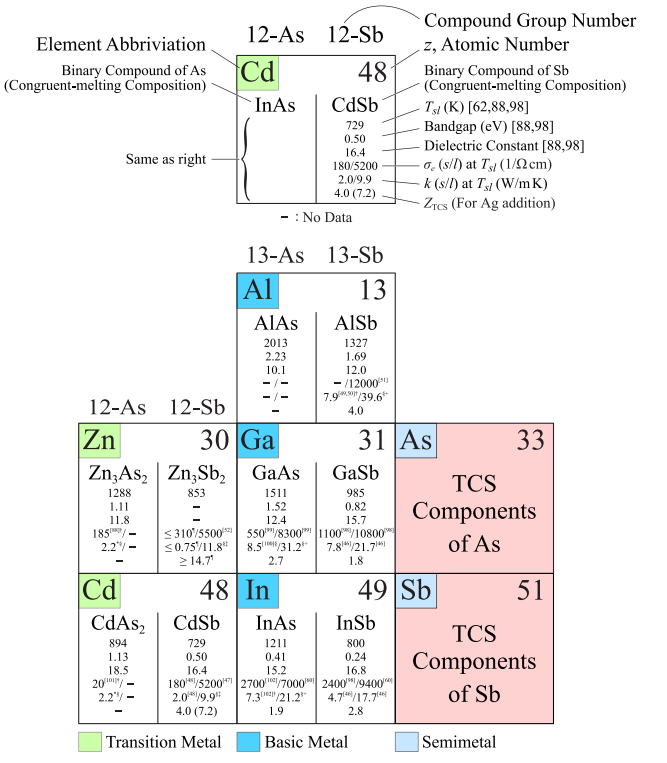

* Slack relation with available data [62,88]
§ W-F law with available σ_e data
† Extrapolation from data
‡ k_l is calculated by Bridgman theory [1] using measured speed of sound and molar volume [103,104]
⁺ k_l is calculated by Bridgman theory [1] using bulk modulus obtained by *ab initio* calculations (see section V)
¶ Expected values (see Section VII)

FIG. 5. Periodic table for binary TCS compounds based on As and Sb. The incongruent melting compounds are excluded. The TCS-related properties of the compounds are listed. There are periodic trends for properties and CdSb and Zn_3Sb_2 stand out. The As compound data are rare due to their reactivity and toxicity.

liquid alloys with $\sigma > \sigma_{\text{limit}}$ are NFE metals (ideal metallic behavior), but the liquid CdSb has a semiconductor behavior of the σ_e, even though $\sigma_e > \sigma_{\text{limit}}$ [47].

The electronic localization function (ELF) and the charge density distribution present clues for evaluating the behavior of valance electrons of materials in terms of the local-/delocalization. As shown in Fig. 4, the localized electrons can be seen as the formation of bond attractors in the ELF and the overlapped charge density distributions between atoms in semiconductors, whereas the network of channel which encloses the attractors in the ELF and the spherical charge density distribution stand for the metallic behavior (see Sec. VI). The origin of the $\Delta E_{e,g}$ is the local-/delocalization of valence electrons (due to the nature of orbitals and its contribution to the bonding). As shown in Figs. 11 and 12, the S/M transition of CdSb is mainly due to the $5p$ orbital of Sb atom, the same as the semimetal/metal transition of elemental Sb (see Sec. VI). Considering binary semiconductor compounds including CdSb, it is expected that the combinations of metal and semimetal/semiconductor elements provide the p orbital (S/M transition) for high Z_{TCS}. Investigation for existing materials shows six compounds with the $Z_{\text{TCS}} \geqslant 1.8$, i.e., elemental Ge and Si; CdSb, InSb, $Ge_2Sb_2Te_5$, GaSb, and AlSb, in Fig. 2. The most interesting feature is that all the compounds possess Sb as a base element. Also, all of them except $Ge_2Sb_2Te_5$ are the binary Sb compounds with metallic elements. Therefore, it is believed that Sb is one of the most promising semimetal/semiconductor elements for binary TCS materials, and we call such elements the TCS base element.

To determine possible TCS base elements, the metalloid elements (B, Si, Ge, As, Se, Sb, and Te) are searched for large Δk upon melting. The usual Boron-based semiconductors are III-V compounds (BN, BP, BAs, and BSb) with significantly high k_p; the *ab initio* calculation result [81] shows that their k_p's are higher than 500 W/m K at room temperature and that of BAs is comparable to that of diamond, due to their strong bond, which yields large T_{sl} and T_{D}. So, they cannot possess high Z_{TCS}. The available data show that Se and Te are not suitable since the highest liquid σ_e among most telluride and some selenide semiconductors is less than $3000\,(\Omega\,\text{cm})^{-1}$, and many selenide compounds remain semiconductors upon melting [60]. In the report [60], it is mentioned that the chemical binding remains strong and they cannot be considered as the system of free-electron model, similar to CdSb but with much lower σ_e. So, selenides and tellurides do not have a large σ_e jump upon melting. The common binary semiconductor compounds of Si or Ge are SiSe, $SiSe_2$, GeSe, $GeSe_2$, and GeTe. As discussed, the GeSe is a liquid semiconductor and the highest liquid σ_e of GeTe is $<3000\,(\Omega\,\text{cm})^{-1}$ [60]. The σ_e of Ge-Se system decreases as the Se composition increases [82], so $GeSe_2$ is also a liquid semiconductor. Also, the liquid σ_e of the SiSe and $SiSe_2$ are almost close to those of the GeSe and $GeSe_2$, respectively, which implies that the SiSe and $SiSe_2$ are also semiconductors [83]. There is no congruent melting composition for the binary compounds of Si or Ge with metal elements in groups 12–15 [84]. Therefore, the Si and Ge can be excluded from the TCS base elements. The remaining metalloid elements are the As and Sb, and they do not make a distinct binary compounds with congruent melting [84]. It is expected that As would be TCS base element, the same as Sb since both are semimetals in group 15.

Figure 5 lists properties of binary compounds (with congruent melting) based on the As and Sb with metal elements in groups 12–15. The metallic elements in the sixth row (Hg-Bi) are not included because they do not form a distinct congruent melting compound (the As-Hg phase diagram is unknown [85]) [62]. Sn compounds are also excluded because there is no congruent melting compound in the Sn-Sb system [62] and congruent melting compounds of the Sn-As system [62] (SnAs and Sn_4As_3) are metallic [86,87]. Although $ZnAs_2$ and Cd_3As_2 are congruent compounds in each system, the $k(s)$ of $ZnAs_2$ is much higher than that of Zn_3As_2 due to the significantly small Grüneisen parameter [88], and the Cd_3As_2 is a metallic solid with the high σ_e at room temperature [88,89].

Considering the group 13-Sb compounds from InSb to AlSb (upward), their T_{sl} increases since the bond is strengthened with lighter elements, so the band gap and T_{D} should increase. Because they have the same lattice structure [62], their Grüneisen parameters are expected to be similar, so their k_p should increase from InSb to AlSb. The contrary trend is in solid σ_e decreasing due to ε_e and band gap; the decrease in the ε_e implies the increase in the Coulomb attraction and the weaker dielectric screening, so σ_e decreases. Although there is no data for the solid σ_e of AlSb, it should be lower than that

of GaSb. So, the electron contribution to the $k(s)$ decreases, whereas the lattice contribution increases. However, the liquid σ_e increases due to the same trend as the solid and liquid σ_e of each pure element ($\sigma_{e,\mathrm{Al}} > \sigma_{e,\mathrm{Ga}} > \sigma_{e,\mathrm{In}}$) [53], and the liquid k_e increases notably since the T_{sl} also increases (W-F law). Because k_f is negligibly small, dominant contribution to $k(l)$ is k_e. So, AlSb has a high Z_{TCS} about 4.0, although it has a significantly large contribution from k_p and high T_{sl}. The reason for the lowest Z_{TCS} of GaSb among them is that both k_p and k_e are not negligible, so $k(s)$ is almost the same as that of AlSb.

The group 13-As compounds have the same trends for properties as those of the 13-Sb compounds: increasing T_{sl} and band gap and the decreasing ε_e. Also, the solid σ_e decreases and the liquid σ_e increases (no data for AlAs). These uniform trends are due to the same composition with same elemental group. The other important trend is that the σ_e of 13-As at liquid are lower than those of 13-Sb (the solid σ_e is lower or similar) due to higher liquid σ_e of elemental Sb compared to that of As [53,90]. So, it is expected that the $k(s)$ of AlAs is higher than that of GaAs due to increase in k_p (but negligible decrease in k_e) and a liquid σ_e much lower than AlSb, so Z_{TCS} not higher than AlSb (4.0). The reason for the higher Z_{TCS} of GaAs compared to InAs (not the same trend as the 13-Sb) is a much lower electrical contribution to $k(s)$ for GaAs (low solid σ_e), so they have similar $k(s)$. Therefore, the highest Z_{TCS} material in group 13 is the AlSb, the same Z_{TCS} as pure CdSb.

The $CdAs_2$ is a possible TCS in the Cd-As system, but its predicted $k(s)$ is slightly larger than CdSb, and it is expected that its liquid σ_e is lower than CdSb (due to high As content and higher σ_e for antimonides compared to arsenides). So Z_{TCS} of $CdAs_2$ should be lower than CdSb (the data for $CdAs_2$ is limited). Also, CdSb can have higher Z_{TCS} with Ag addition, as discussed. Similarly, liquid σ_e of Zn_3As_2 will be smaller than Zn_3Sb_2. However, most of Zn_3Sb_2 properties are not known [91,92]. Since $k(s)$ of β-Zn_4Sb_3 [93] is much smaller than Zn_3As_2 and $k(s)$ of Zn_3Sb_2 is not expected to be higher (see below), Z_{TCS} of Zn_3As_2 is smaller than Zn_3Sb_2. The reason for the low $k(s)$ of CdSb and β-Zn_4Sb_3 (essential to the high Z_{TCS}) is their electron-poor nature [48,91]. Since there are 3.5 electrons per atom, the weak multicenter bonds are formed in CdSb to make up for this, leading to nonuniform atomic bonds and the strong anharmonicity [48,94]. The main structure of β-Zn_4Sb_3 is the rhombohedral $Zn_{36}Sb_{30}$ with an electron deficiency, so the balance is corrected by the interstitial Zn atoms which yield disorder as defects and the soft and anharmonic bonding [91,95,96]. Therefore, the $k(s)$ of CdSb and β-Zn_4Sb_3 are rather low. Similarity is expected between β-Zn_4Sb_3 and Zn_3Sb_2. Whereas β-Zn_4Sb_3 has three interstitial Zn atom sites (36 available positions for each site) in the unit cell [95], there are 18 Zn atom sites (8 available positions for each site) in Zn_3Sb_2 (with larger unit cell) and only one of them has the full occupancy [97]. So, a more disordered structure with a stronger anharmonic bonding is expected for the Zn_3Sb_2, and thus the $k(s)$ of Zn_3Sb_2 would not be higher than β-Zn_4Sb_3.

From the discussions above, Sb is the best TCS base element due to its anharmonic bonding characteristics with group 12 elements, and higher liquid σ_e of antimonides than arsenides, leading to high Z_{TCS}. Among antimonides, Zn_3Sb_2 and CdSb have high Z_{TCS}. We discuss and analyze related properties of CdSb in Sec. VI and Zn_3Sb_2/β-Zn_4Sb_3 in Sec. VII.

V. *AB INITIO* CALCULATION METHOD

The *ab initio* calculations are implemented by the Vienna *ab initio* Simulation Package (VASP) [105] and the ABINITpackages [106,107]. The VASP is used for the relaxation of atomic structures, electron density of states (D_e) and band structures, ELF, *ab initio* molecular dynamics (AIMD), and bulk modulus. The Perdew-Burke-Ernzerhof (PBE) [108] exchange-correlation functional is used along with the projector augmented wave (PAW) method [109,110] with 300-eV cutoff energy. The DFT-D3 method [111,112] with the Becke-Johnson damping for the van der Waals correction is adopted to obtain accurate results, since the cleavage planes inside CdSb are interconnected by the van der Waals interaction [48]. The usual density functionals are unable to describe the van der Waals correctly [113], and the calculations can be improved drastically with the van der Waals density functional [114]. In the D_e and band structure calculation, the modified Becke-Johnson (mBJ) exchange potential [115,116] is included with nonspherical contributions from the gradient corrections inside PAW spheres (LASPH = .TRUE., in the VASP tag), since the mBJ often results in aspherical charge densities [113]. Our predicted band-gap energy for CdSb only with PBE functional was very poor, less than 0.1 eV significantly different to the experimental results (about 0.5 eV), and the previous reports [48,94] show that the mBJ can predict the correct D_e and band structure.

For CdSb, the Γ-centered grids with $8 \times 6 \times 6$ $\boldsymbol{k}$ points are used for the relaxation of the atomic structure, and the relaxed structure is used to calculate the D_e with expanded $30 \times 24 \times 24$ $\boldsymbol{k}$ points for accuracy and the band structure with $\boldsymbol{k}$ points along the Brillouin zone edges, but $4 \times 3 \times 3$ $\boldsymbol{k}$ points are used for D_e calculations with a supercell, considering that D_e results for the CdSb supercell do not vary with larger number of $\boldsymbol{k}$ points. For pure Sb, the Γ-centered grids with $13 \times 13 \times 5$ and $33 \times 33 \times 13$ $\boldsymbol{k}$ points are used for the relaxation and the D_e of the solid unit cell and $8 \times 8 \times 3$ $\boldsymbol{k}$ points for the D_e of the liquid supercell. Also, for pure Cd, the Γ-centered grids with $25 \times 25 \times 13$ $\boldsymbol{k}$ points are used for the relaxation of the solid unit cell and $7 \times 7 \times 6$ $\boldsymbol{k}$ points for the D_e of the liquid supercell. For β-Zn_4Sb_3, the Γ-centered grids with $3 \times 3 \times 3$ $\boldsymbol{k}$ points are used for the structure relaxation, considering the large unit cell size and the fact that the relaxed structure with larger number of $\boldsymbol{k}$ points is almost the same.

The AIMD calculation is implemented with canonical ensemble (NVT) under the Nosè-Hoover thermostat at prescribed temperature and a 1-fs time step is used. The Fermi-smearing method is adopted with the smearing width corresponding to the energy at prescribed temperatures. The only Γ point is used for the AIMD [117,118], and four snapshots are collected from the AIMD results at every 1 ps after reaching equilibrium (3 ps) to calculate properties of liquid phase [118,119]. The thermodynamic relation of the bulk modulus is $E_p = V_o(dP/dV)$, where V_o is the zero-pressure volume. The pressure data from the AIMD calculations for various volumes are used to obtain the V_o and the derivative of P with respect to

V and to calculate the E_p, by following the method suggested [120].

The ABINIT package with CONDUCTI code [121,122] embedded in the package is used to predict the real part of the σ_e for liquid CdSb by calculating the Kubo-Greenwood (K-G) formula [123,124] written as [118]

$$\sigma_e = \frac{he_c^2}{V}\sum_{\boldsymbol{k}',\boldsymbol{k}}\lim_{E\to 0}\frac{f(E_{\boldsymbol{k}'})-f(E_{\boldsymbol{k}})}{E} \times \delta(E_{\boldsymbol{k}'}-E_{\boldsymbol{k}}-E)\langle\psi_{\boldsymbol{k}}|\hat{\mathbf{v}}|\psi_{\boldsymbol{k}'}\rangle\langle\psi_{\boldsymbol{k}'}|\hat{\mathbf{v}}|\psi_{\boldsymbol{k}}\rangle, \quad (4)$$

where h is the Planck constant, $E_{\boldsymbol{k}}$ is energy (eigenvalue) of eigenstate $\boldsymbol{k}$, $f(E_{\boldsymbol{k}})$ is Fermi-Dirac occupancy function, $\psi_{\boldsymbol{k}}$ is wave function of eigenstate $\boldsymbol{k}$, and $\langle\psi_{\boldsymbol{k}}|\hat{\mathbf{v}}|\psi_{\boldsymbol{k}'}\rangle$ is velocity matrix elements. The δ function ensures the energy conservation of electrons, and the $\hat{\mathbf{v}}$ can be expressed by Hamiltonian gradient as [118]

$$\hat{\mathbf{v}} = \frac{1}{\hbar}\frac{\partial \mathrm{H}}{\partial \boldsymbol{k}}. \quad (5)$$

The calculations are implemented with snapshots obtained by the VASP AIMD calculations for each temperature. The PBE exchange-correlation functional is used along with PAW method, with 408 eV (15 Hartree) cutoff energy and $2\times2\times2$ $\boldsymbol{k}$ points of a Monkhorst-Pack grid. Our tests showed that results were not affected by further increases in cutoff energy and $\boldsymbol{k}$ points. The δ function is treated by the Gaussian function with the broadening width of 0.03 Ha following the suggested method [125], and the well-converged σ_e can be obtained without any unphysical fluctuations along frequencies.

VI. HIGH Z_{TCS} CdSb

A. Atomic structure of CdSb

Solid CdSb has a small $\Delta E_{e,g}$ (0.5 eV) [94], very low phonon cutoff energy (21 meV) [48,126], and its orthorhombic unit cell consist of 8 Cd and Sb atoms each having five neighbors, whereas there are only two Cd-Sb bonds for Cd atoms and two Cd-Sb and one Sb-Sb bond for Sb atoms within the sum of covalent radii for Cd (1.44 Å) and Sb (1.39 Å), respectively [48,127]. The $sp3$ hybridization has been suggested, but Ashcheulov *et al.*[128] claims inequivalent hybrid orbitals as linear combinations of s and p orbitals. Using the electron-localizability indicator (ELI-D), Wang *et al.*[48] shows there are a collection of three covalent bonds (two-center bonds) and one three-center interaction (Cd-Sb-Cd), i.e., a shared lone electron pair and inducing the interlayered structure with anisotropic properties. They explained the existence of the three-center interaction is from the deficiency of valence electrons (3.5 electrons per atom).

The *ab initio* calculated structure is presented in Fig. 6, showing nonuniform atomic bonds and angles and anisotropy more accurately than previous reports [48,94] because the van der Waals interactions are included (Table I). Figure 6(a) shows that the contours of charge density distribution around Sb atoms is distorted (rounded triangular or tetrahedron), but around Cd it is spherical (slightly distorted) and Cd and Sb contours overlap due to the Cd-Sb covalent bonds. Figure 7 shows the structures of Cd and Sb, where the charge density distribution around Cd is spherical and around Sb is also

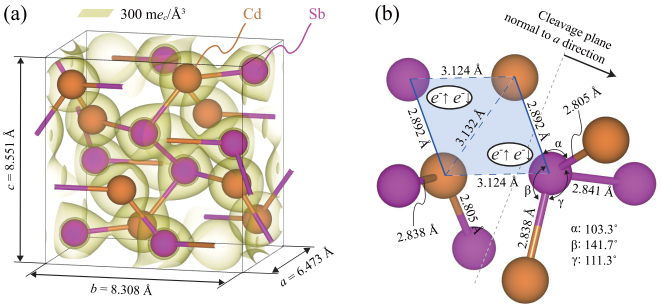

FIG. 6. *Ab initio*-predicted structure of CdSb. (a) Orthorombic unit cell of solid with the charge density distribution. The contours are for 300 $\mathrm{me_c/\AA^3}$, and the covalent bonds are marked as rods. (b) Bond lengths and angles are also shown. A pair of electrons shared in the three-center interaction (Cd-Sb-Cd) is highlighted. The predicted lattice constants, bond lengths, and angles are in good agreement with experiments (Table I).

spherical but linked between atoms. The bond length of Cd and Sb is 2.96 and 2.93 Å, respectively, larger than the covalent bonds. Considering the charge density distributions and bond lengths, these imply that valence electrons of Cd are localized with those of Sb forming covalent bonds.

CdSb is the only stable one in the Cd-Sb system under phase transition [128], i.e., congruent melting (T_{sl} = 729 K). In the melt CdSb, clusters of short-range order remain [130], consisting of Cd_xSb_y, implying strong interactions (Cd-Cd or Sb-Sb clusters are not possible [130]). The softening effect by melting is weak and the difference between the k_p and the k_f will be small. The liquid CdSb is rather isotropic with free-electron-like transport properties [60,131,132]. Some bonds (especially shared electron pairs and Sb-Sb) dissociate upon melting and some unbound valence electrons become delocalized and wander, i.e., metal-like.

AIMD calculations verify the liquid properties at 800 K, using a $2\times2\times2$ supercell (128 atoms) and the density of the liquid supercell is set the same as solid (actual 1% density difference [103,133] is comparable to relaxation error in Table I). Figure 8 is a snapshot of liquid CdSb at 800 K

TABLE I. Atomic structure properties of CdSb predicted by *ab initio* calculations and compared with experiments [48,129]. The maximum difference is 1.1%.

Parameters	*Ab initio*	Previous reports	Error (%)
Lattice constants (Å)	$a = 6.473$	$a = 6.469$	0.06
	$b = 8.308$	$b = 8.251$	0.69
	$c = 8.551$	$c = 8.522$	0.34
Bond length, Cd-Sb (Å)	2.805	2.793	0.43
	2.838	2.824	0.50
	2.892	2.882	0.35
	3.124	3.127	0.10
Bond length, Sb-Sb (Å)	2.841	2.810	1.10
Bond length, Cd-Cd (Å)	3.132	3.136	0.13
Angle, Cd-Sb-Cd (deg.)	$\alpha = 103.3$	$\alpha = 103.9$	0.58
	$\beta = 111.3$	$\beta = 110.4$	0.82
	$\gamma = 141.7$	$\gamma = 141.4$	0.21

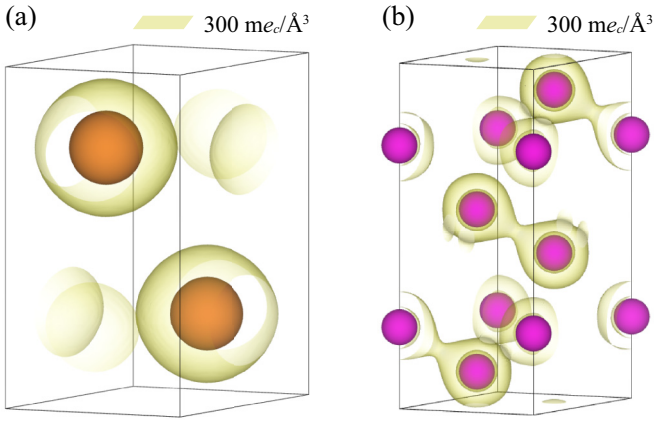

FIG. 7. Charge density distributions of the solid (a) Cd and (b) Sb unit cells, predicted by *ab initio* calculations. The contours are for 300 $me_c/Å^3$. The shortest Cd-Cd and Sb-Sb separations are 2.96 and 2.93 Å, respectively. The result shows that the charge density distribution of CdSb (Fig. 6) is noticeably transformed, implying covalent bonding.

with charge density distribution and most Cd show spherical distribution without overlaps, indicating metallic bonding and properties [134]. The charge density distribution around Sb is less distorted and most of its covalent bonds are dissociated, so its delocalized electrons contribute to transport.

B. Electronic structure of CdSb

The S/M transition features are described by the charge density distributions combined with the ELF, which suggests classification of bonding based on the topological analysis [135]. The value of ELF is between 0 and 1, where 1 and 0.5 correspond to perfect localization and uniform electron gas [135,136]. The localization attractors are defined by the local maxima of local functions related to the Pauli exclusion principle and there are bonding and nonbonding attractors. The bonding attractors have point or circular shapes and indicate that the localized electrons are involved in bonds, whereas the nonbonding attractors have ring shapes. The metallic bonds form a three-dimensional (3D) network (trajectories) connecting all attractors as the ELF level decreases [135]. The metallicity identification may not always be reliable using the ELF; diamond carbon [136] and lithium [135] both show bond attractors at high ELF levels and a network of channels at low ELF levels. Here, with focus of the TCS on the S/M transition upon melting, there is almost no bond attractor in metallic liquids, so the discussion regarding metallicity of the liquid phases using the ELF is rather valid (see the CdSb as an example below). Although the solid CdSb does not show a network of channels, it is possible that the solid phases of other notable TCS materials do. In that case, the density of states (DOS) should also be examined to confirm a nonmetallicity.

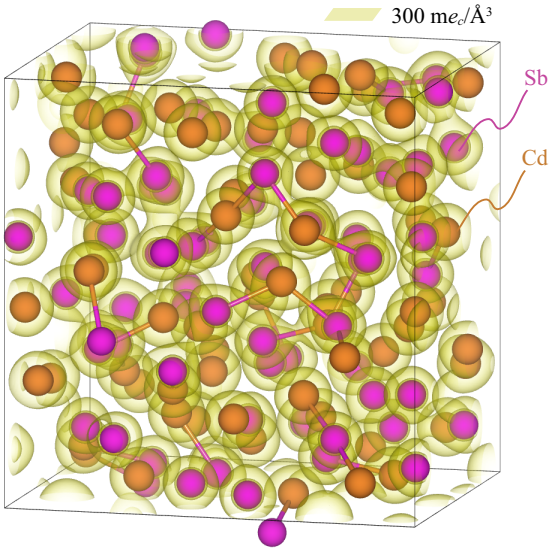

FIG. 8. Atomic structure of liquid CdSb at 800 K after 6 ps of AIMD calculations, along with the charge density distribution. The contours are for 300 $me_c/Å^3$. The structure is random, and the overlapping isosurface region is significantly reduced. The Cd_xSb_y clusters with bond lengths smaller than 2.9 Å are marked with rods.

Figure 9 shows the ELF contours for solid CdSb, and the reducible localization domain, where the attractors merged within two neighboring Sb, is seen in Fig. 9(a). The network is formed within only one Sb-Sb bond, indicating that CdSb cannot be metallic. As the ELF level increases, the bifurcations of attractors occur at a critical value [135], and Sb-Sb bond attractor begins to separate at the critical level of 0.74. The Sb-Sb bond attractor is located in the middle point of Sb-Sb bond, suggesting that electrons forming a covalent bond are localized [Fig. 9(b)]. The attractors for Cd-Sb bonds and Cd-Sb-Cd interaction (van der Waals) are fully separated at the ELF level of 0.835 [Fig. 9(c)]. All attractors are located on the bonding line [135] and are much close to Sb [128], since the electronegativity of Sb (2.05) [1] is larger than Cd (1.69) [1] (electrons localized close to Sb). Two van der Waals attractors are very close to each other and facing partner (Cd), but contours are nonuniform; the van der Waals attractor with shorter interaction distance (2.892 Å) is much larger than the longer distance (3.124 Å). The shared lone electron pair in Cd-Sb-Cd interaction is more probable to be located near a Cd, leading to stronger van der Waals interaction and a closer, shorter bond.

Contrary to solid bond characteristics, the liquid attractors [Fig. 10(a)] around Sb are ring type (not intact due to disorder), similar to nonbonding ring attractor [135]. There is no attractor between Sb-Sb pairs with bond length 2.647 Å [smaller than two times covalent radius of Sb (2.78 Å)] in Fig. 10(a). There are Cd_xSb_y clusters in liquid; the Cd-Sb pair with long bond length 3.082 Å forms the bond attractor between them (close to Sb). Based on the length, it may not be a covalent bond, but shows Cd-Sb interaction [130]. Figure 10(b) shows the liquid metallic behavior with a 3D network connecting all attractors around Sb [135]. The ELF contours around the Sb-Sb pair with 2.647 Å [Fig. 10(a)] become closer as the ELF level decreases and finally merge each [Fig. 10(b)], but the bonding attractor between them is never formed. The ELF results suggest that liquid CdSb is metallic.

The band structure and solid and liquid D_e from *ab initio* calculations are shown in Fig. 11. The highest-edge valence and lowest-edge conduction band are near the X and Z

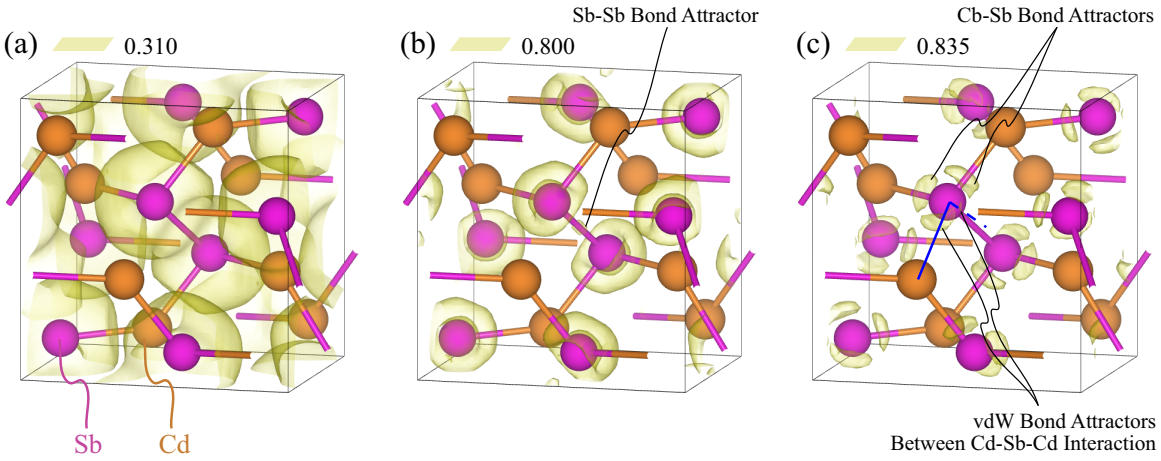

FIG. 9. The ELF for solid CdSb unit cell showing the contours with the level of (a) 0.310, (b) 0.800, and (c) 0.835. The blue lines coincide with those in Fig. 6(b), and the broken bonds indicate bonding with adjacent cell. The reducible localization domain which merged bond attractors within nearest two Sb atoms in (a) begins to separate as the ELF level increases (bifurcation), and the attractors for Sb-Sb bond can be seen in (b) and for Cd-Sb bonds and Cd-Sb-Cd interaction in (c).

points, and the solid band gap of 0.49 eV is consistent with experiments/predictions [48,94]. The solid D_e shows that the $4d$ of Cd is intensely overlapped with $5s$ orbital of Sb, within deep electron energy states (-11 to -7 eV), similar to liquid Hg [137] (group 12 feature). These states consist of four narrow energy bands with high peaks and some narrow band gaps between them, and the band with the largest peak is significantly contributed to Cd $4d$ (near -9 eV). So, these four peaks originate from Cd-Sb and Cd-Cd interactions and related electrons are localized in these deep bands. Many valence electrons are from Cd $4d$, so the band with the Cd-Cd interaction has the highest peak.

There are two wide conduction and valence bands up and down from both gap ends and the Sb $5p$ makes the largest contribution to these bands, especially to upper side of the valence band, and also contributions of Cd $5s$ and $5p$ to those bands can be seen [48]. These bands are mainly originated from the Sb-Sb bond, but the couplings of the Sb $5p$ with the Cd $5s$ and $5p$ through Cd-Sb also affect to the formation of valence and conduction bands, especially the Cd $5s$ for lower parts of valence and conduction bands and the Cd $5p$ for upper parts. The interactions between Sb-Sb and Cd-Sb contribute to the prohibited band-energy region, but not the interaction between Cd atoms.

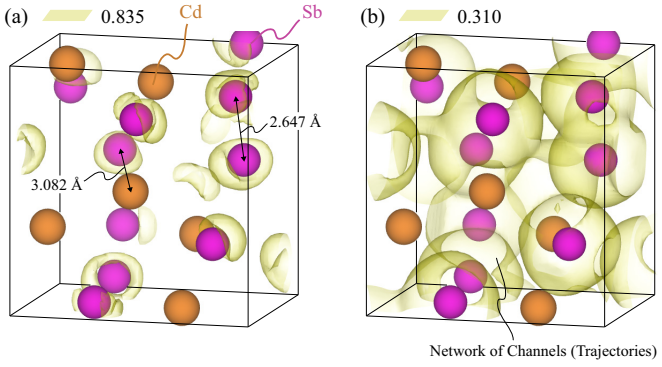

FIG. 10. The ELF for liquid CdSb supercell showing contours with the level of (a) 0.835 and (b) 0.310. The partial volume of supercell, the same as that of solid CdSb unit cell, is presented for comparison to the solid ELF of Fig. 9. The bond lengths for two atom pairs are presented in (a) to show the different bond characteristics of solid and liquid. All attractors near the Sb atoms in (a) are merged into the reducible localization domain with the low ELF level in (b), forming a three-dimensional network.

The liquid CdSb D_e at 800 K in Fig. 11(b) is obtained by averaging of the snapshot results and shows that the valence and conduction bands merged and the band gap disappears (metallic). The highest contribution near the Fermi level is the Sb $5p$; the valley of partial Sb $5p$ D_e is fully represented to total D_e. Figures 12(a) and 12(b) show solid and liquid (950 K) Sb D_e, with the main contribution to the metallic transition upon melting from the $5p$ orbital and the partial D_e of other orbitals barely changing. The phenomenon is similar to the changes in partial Sb D_e in CdSb upon melting. Also, the valley in Fig. 11(b) is observed in Fig. 12(b). The valence electrons of the Sb $5p$ orbital, once localized in the solid state by the interactions with the Cd $5s$ and $5p$ orbitals and the $5p$ orbital of other Sb atoms, are delocalized, and these electrons contribute to the metallic behavior of the liquid. Also, the Cd partial D_e's in liquid CdSb are similar to those of liquid Cd [Fig. 12(c)], confirming that sole Cd contributes to the liquid metallic properties. Although gradual increase in $5s$ and decrease in $5p$ partial D_e of liquid Cd are observed, the shallow valleys in the partial D_e of Cd $5s$ and $5p$ can be found in compound [Fig. 11(b)]. This implies that not all Cds behave like liquid but some of them are engaged in Cd_xSb_y clusters.

C. Transport properties of CdSb

The CdSb $k(s)$ decreases up to 425 K, then increases, as reviewed in Fig. 3 [48,138]. Following the Slack relation (T^{-1}) [1], this increase is due to k_e and/or k_{e+h}; however, k_e is very small (about 0.2 W/m K [48]), so this is due to k_{e+h}. The thermal conductivities of the solid and liquid CdSb are obtained by the theoretical treatments, and each contribution is shown in Fig. 13. The k_f is derived from the kinetic

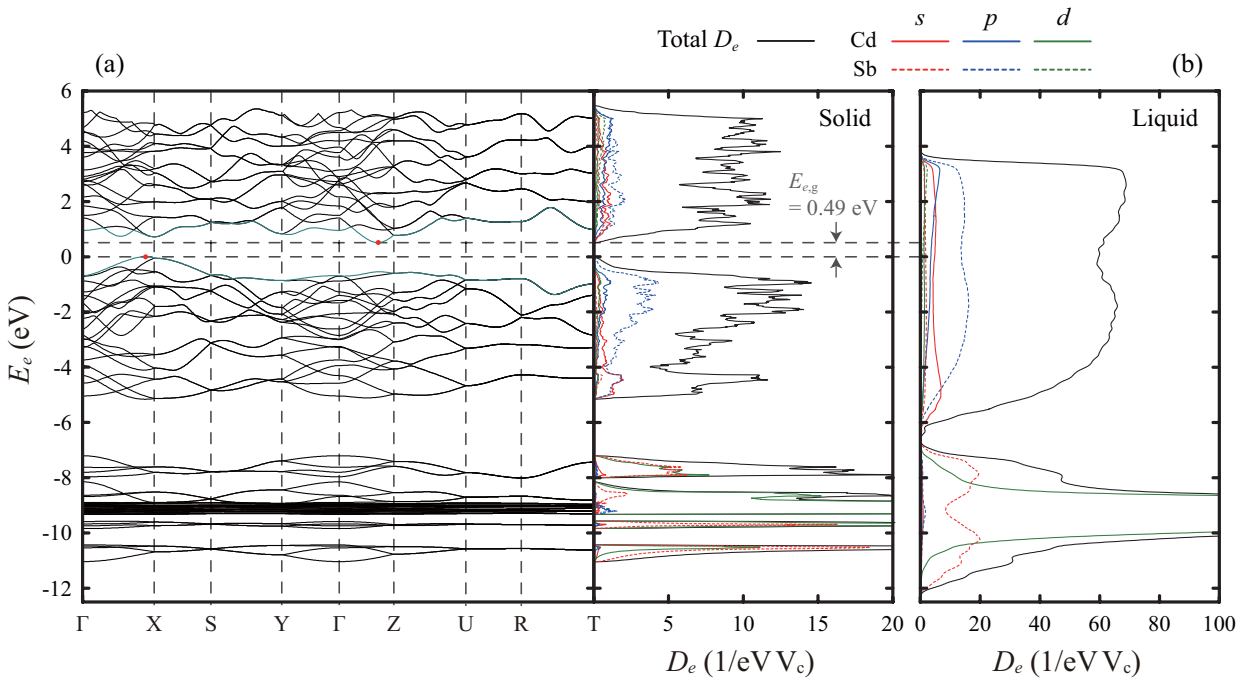

FIG. 11. (a) Electronic band structure (the Fermi energy is set to be zero) and D_e of solid CdSb unit cell. The highest occupied and the lowest unoccupied bands are colored, and red dots are the edges of them. (b) The D_e of liquid CdSb supercell calculated with atomic structures from the AIMD results at 800 K. The liquid D_e is averaged over four snapshots, but results are very similar. Contributions of orbitals of constituent atoms (partial D_e) are also shown. The partial D_e is obtained within Wigner-Seitz radius, so the sum of partial D_e is not equal to the total D_e. The band gap disappears in the liquid phase, i.e., metal upon melting.

theory [1]

$$k_f = \tfrac{1}{3}\rho_f c_{v,f} a_s \lambda_f, \tag{6}$$

where ρ_f is the fluid density, $c_{v,f}$ is specific heat at constant volume, a_s is speed of sound in liquid, and λ_f is mean free path of fluid molecules. The Bridgman theory treats liquid as a simple cubic arrangement of atoms with its mean free path equal to the three times of mean atomic spacing, i.e. [1],

$$k_f = \rho_f \frac{3R_g}{M} a_s \left(\frac{M}{\rho_f N_\mathrm{A}}\right)^{1/3} = \frac{3R_g}{N_\mathrm{A}^{1/3}} \frac{\rho_f^{1/6}}{M^{2/3}} \left(\frac{c_{p,f}}{c_{v,f}} E_p\right)^{1/2}, \tag{7}$$

where R_g is the gas constant, M is molecular weight (here in molar base), N_A is Avogadro number, and $c_{p,f}$ is specific heat at constant pressure (usually $c_{p,f} \approx c_{v,f}$ for liquid). The k_f of liquid CdSb estimated as 0.49 W/m K at T_{sl}, with $M = 234.17$ g/mol, $a_s = 1748$ m/s, and $\rho_f = 6.857$ g/cm^3 [103], so in TCS, k_f is small, making negligible contribution compared to k_e.

The Slack relation $k_{p,\mathrm{S}}$, which is extended from the Leibfried and Schlömann equation for complex lattices [139], is [1]

$$k_{p,\mathrm{S}} = \frac{3.1 \times 10^4 \langle M \rangle V_a^{1/3} T_{\mathrm{D},\infty}^3}{T \langle \gamma_\mathrm{G}^2 \rangle N_o^{2/3}}, \tag{8}$$

where $T_{\mathrm{D},\infty}$ is the high-temperature Debye temperature, $\langle \gamma_\mathrm{G}^2 \rangle$ is mode averaged square of the dimensionless Grüneisen parameter at high temperature, and N_o is number of atoms in the primitive cell. The $T_{\mathrm{D},\infty}$ and $\langle \gamma_\mathrm{G}^2 \rangle$ can be replaced with T_D and $\langle \gamma_\mathrm{G} \rangle^2$, respectively. The properties $\langle M \rangle = 117.058$ g/mol, $V_a = 1/n$ ($n = N_o/abc$, where $a = 6.469$ Å, $b = 8.251$ Å, and $c = 8.522$ Å are lattice constants from the experiment [129] and $N_o = 16$), $T_{\mathrm{D},\infty} = 180$ K, and $\langle \gamma_\mathrm{G} \rangle = 1.82$ are used [94,140]. The k_p within 300 K–400 K is coincident with $k(s)$ from the experiment due to negligible k_e and k_{e+h} at low temperatures. Though the Slack relation underestimates k_p at high temperatures due to its simplicity (T^{-1}), $k_f > k_p$ (0.42 W/m K) at T_{sl}. Therefore, The actual decreasing rate of k_p with temperature is slightly lower than the Slack result.

The minimum k_p can be obtained from the Cahill-Pohl model with assumptions of a mean free path of phonon equal to one half of wavelength, no phonon dispersion, and dominant short length-scale interactions [1], i.e.,

$$k_{p,\mathrm{C\text{-}P}} = \left(\frac{\pi}{6}\right)^{1/3} k_\mathrm{B} n^{2/3} \sum_\alpha u_{p,\alpha} \times \left(\frac{T}{T_{\mathrm{D},\alpha}}\right)^2 \int_0^{T_{\mathrm{D},\alpha}/T} \frac{x^3 e^x}{(e^x - 1)^2} dx, \tag{9}$$

where α is the phonon branch, $u_{p,\alpha}$ is phonon velocity, and $T_{\mathrm{D},\alpha}$ is Debye temperature for each branch as

$$T_{\mathrm{D},\alpha} = u_{p,\alpha} \frac{k_\mathrm{B}}{\hbar} (6\pi^2 n)^{1/3}. \tag{10}$$

The acoustic phonon velocities are $u_{p,\alpha} = 1300$, 1581, and 2988 m/s for two transverse and one longitudinal phonons in the vicinity of Brillouin zone center (no dispersion) [48]. The minimum k_p is almost flat in a wide range of temperature (Fig. 13) after reaching a plateau at $T_{\mathrm{D},\alpha}$ [1] (average of $T_{\mathrm{D},\alpha} = 191$ K). The calculated $k_{p,\min}$ is 0.35 W/m K, the same

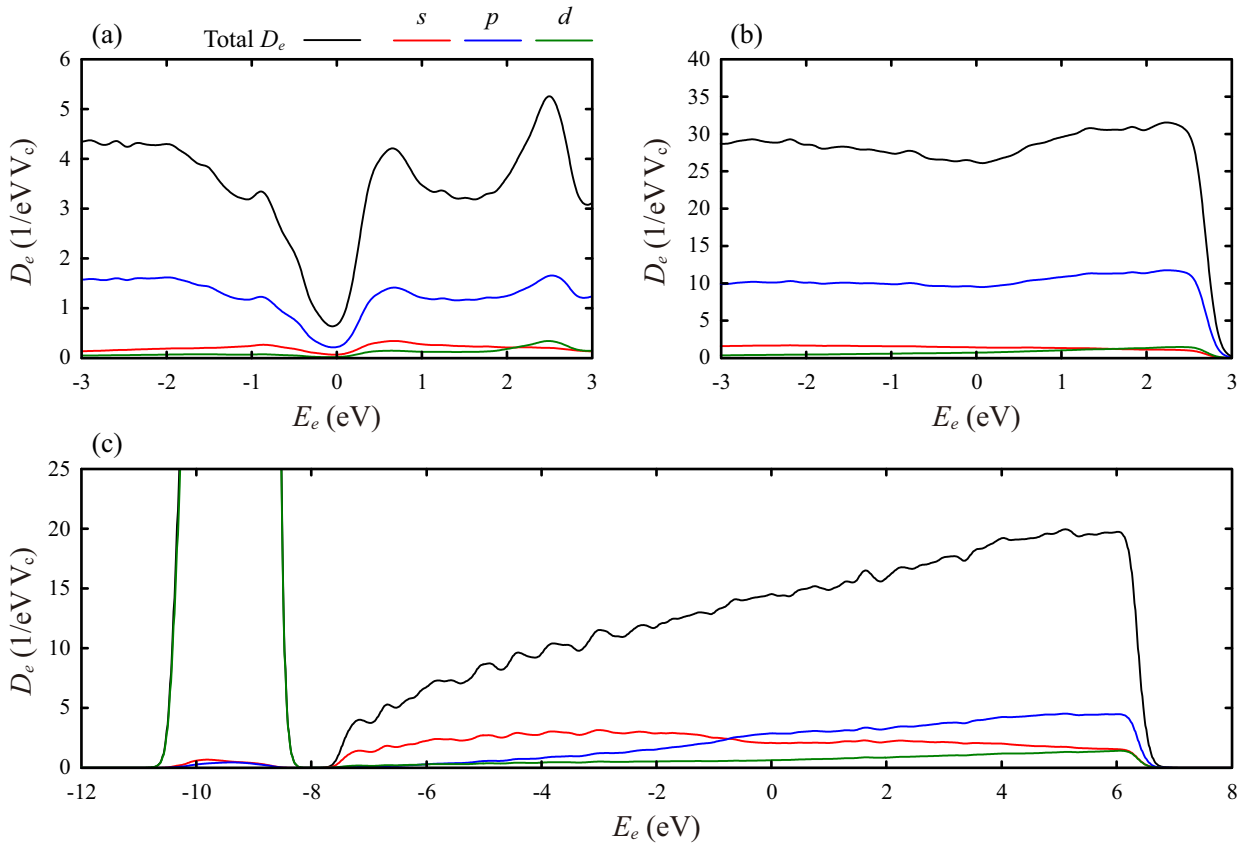

FIG. 12. The D_e of (a) solid Sb (unit cell), (b) liquid Sb ($2 \times 2 \times 2$ supercell at 950 K; $T_{sl} = 904$ K), and (c) liquid Cd ($3 \times 3 \times 2$ supercell at 700 K; $T_{sl} = 594$ K). The Fermi energy is set to be zero. The solid Sb is semimetal, considering the deep valley at 0 eV. After melting, the liquid Sb becomes a metal and the valley almost disappears. It shows that the overlap of charge density distribution between Sb atoms in liquid CdSb does not imply that Sb atoms are forming covalent bonds. The $4d$ orbital of the liquid Cd mainly contributes to the deep electron energy states, whereas both the $5s$ and the $5p$ orbitals of Cd contribute to the states near the Fermi level.

as the reported result [48]. The k_p calculated from Eq. (8) is nearly $k_{p,\min}$ at T_{sl}. This low k_p is caused by the deficiency of valence electrons (3.5 electrons per atom) which results in the complicated structure (Fig. 6). The weak three-center bonding leads to a small force constant and modulus, which lower phonon velocities and T_D, and strong anharmonic branches, which induce a large Grüneisen parameter [48,94]. Also, the strong coupling between soft optical phonon and acoustic phonon enhances scattering and contributes to the low k_p [48,94].

A theoretical model is used for k_{e+h} prediction, i.e. [141,142],

$$k_{e+h} = \frac{\sigma_e \sigma_h}{\sigma_e + \sigma_h}(\alpha_h - \alpha_e)^2 T, \tag{11}$$

where $\sigma_i = n_i e_i \mu_i$ is the electrical conductivity of charge carrier i (carrier charge e_i) and α_i is the Seebeck coefficient. The Seebeck coefficient for a single parabolic band is expressed as [143,144]

$$\alpha_i = \pm \frac{k_B}{e_c}\left[\eta_i - \frac{(\lambda_i + 5/2)F_{\lambda_i+3/2}(\eta_i)}{(\lambda_i + 3/2)F_{\lambda_i+1/2}(\eta_i)}\right], \tag{12}$$

where λ_i is the carrier scattering parameter ($\lambda_i = -1/2$, assuming acoustic phonon scattering), η_i is reduced Fermi energy, and F_β is the Fermi integral of the order of β. The η_i and F_β can be written as [143,145–147]

$$\eta_e = (E_F - E_c)/k_B T, \tag{13}$$

$$\eta_e + \eta_h = -\Delta E_{e,g}/k_B T, \tag{14}$$

$$F_\beta(\eta_i) = \int_0^\infty \frac{x^\beta}{1 + e^{x-\eta_i}} dx, \tag{15}$$

where E_F is the Fermi energy and E_c is conduction band energy. With the assumptions that $(E_e - \mu) \gg k_B T$ (electron energy E_e and chemical potential μ) and μ is analogous to E_F, then n_i can be derived theoretically as [2]

$$n_i = 2\left(\frac{m_{i,e} k_B T}{2\pi\hbar^2}\right)^{3/2} \exp(\eta_i). \tag{16}$$

The $m_{i,e}$ for electrons at conduction band minimum and for holes at valence band maximum toward each direction [148] were averaged by the geometric mean (density of state effective mass [149]) with degeneracy factors of 2 for valence band and 6 for conduction band from band structure [Fig. 13(a)] [94,149,150]. The temperature-dependent band-gap energy (-6×10^{-4} eV/K and 0.45 eV at room temperature) [79] was used with constant Fermi level position (0.032 eV/0.46 eV) [151], and μ_i was extrapolated from the measured data (100 K–280 K) [152] and mobilities of hole and electron are the same [153]. The extrapolated μ_i has the temperature

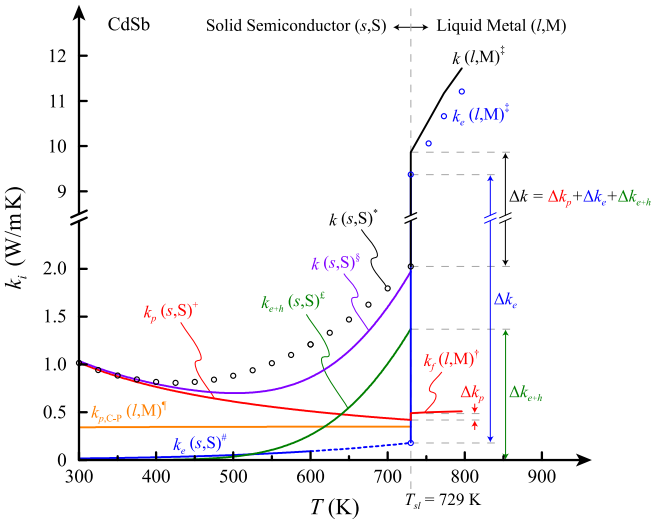

* Experimental result [48] by measured properties ($k = \alpha\rho C_p$) up to 600 K, and extrapolated up to T_{sl}
+ Predicted by the Slack relation [1] with measured properties [129,140] and calculated Grüneisen parameter [94]
¶ Minimum k_p calculated by Cahill-Pohl model using measured lattice constants [129] and predicted phonon velocities [48]
# Experimental result [48] by W-F law using measured σ_e up to 600 K, and extrapolated up to T_{sl}
£ Predicted by the theoretical model (see text)
§ Calculated by $k = k_p(s,S) + k_e(s,S) + k_{e+h}(s,S)$
† Calculated by Bridgman theory [1] using measured speed of sound and molar volume [103]
‡ k_e is Calculated by W-F law using suggested σ_e [47], and k (l,M) = k_f (l,M) + k_e (l,M)

FIG. 13. Temperature dependence of the thermal conductivities of solid and liquid CdSb. The high Z_{TCS} is observed during the S/M transition. The k_e is estimated from the measured σ_e, whereas k_p, k_f, and k_{e+h} are calculated using the theoretical models. The predicted and experimental (black circles) results for $k(s)$ are also compared.

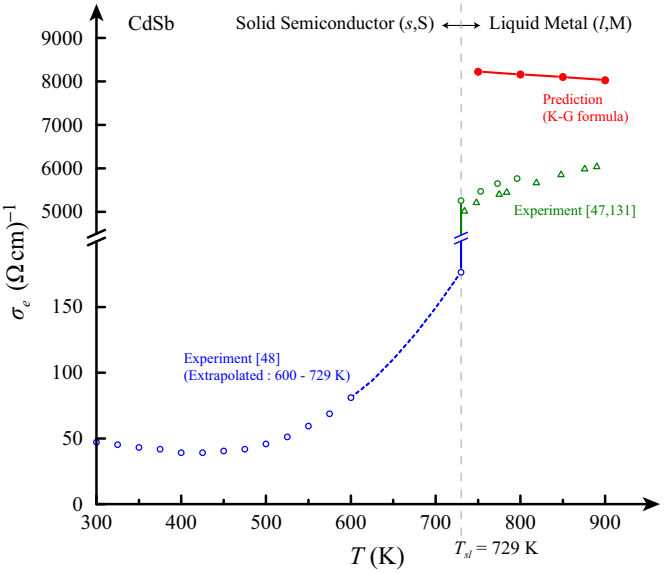

FIG. 14. Temperature dependence of the σ_e for solid and liquid CdSb. The significant rise in σ_e (high Z_{TCS}) is observed during the S/M transition at T_{sl}. The liquid σ_e increases with temperature, due to some remaining short-range order interactions (Cd_xSb_y clusters). The discrepancy between the experiment and the *ab initio* prediction for σ_e is due to the assumptions in the K-G formulation (ideal metallic transport).

dependence of $T^{-1.4}$ consistent to previous claims ($T^{-1.5}$) [154], and is about 350 cm^2/V s at 300 K similar to the measured mobility (300 cm^2/V s at 300 K) [155]. The estimated $k(s)$ is similar to the reported result [48] at the low temperatures (<450 K) and near T_{sl}, but the difference is observed in intermediate temperatures. The reason is because of the steep increase in k_{e+h} estimated; actual k_{e+h} will increase gradually from 400 K, and the discrepancy would occur due to the μ_i extrapolation in a wide range of temperature (300−T_{sl}, lack of data). We believe that the result can be improved with precise mobility data, and k_{e+h} prediction is meaningful for distinguishing and assessing each contribution to $k(s)$.

The solid σ_e starts increasing near 400 K (thermal excitation of electrons) and is about 180 $(\Omega\,\text{cm})^{-1}$ at T_{sl} (Fig. 14), equivalent to 0.2 W/m K. The liquid σ_e is about 5.2×10^3 $(\Omega\,\text{cm})^{-1}$ at T_{sl} [47,60] in the metallic regime [80] and equivalent to 9.4 W/m K. Although its electronic properties like Hall coefficient and thermoelectric power are metallic [131], the semiconductor behavior of liquid σ_e (increasing with temperature) is observed due to the short-range order interactions in low-temperature liquid CdSb [60]. The liquid σ_e increases as a logarithmic function (Fig. 14); semiconductor behavior becomes weak and the short-range interactions reduce as temperature increases [156]. Thus, liquid σ_e will start decreasing eventually when the clusters of short-range order totally disappear and metallic behavior begins. The previous reports [128,157] indicate that it occurs at 773 K, so there is a contradiction with the experiment [47]. We believe that the disappearance point is higher than 890 K because of the evidence for the presence of clusters in liquid D_e at 800 K [Fig. 11(b)]. Also, the data [156] shows that liquid specific heat is higher than predictions by the Neumann-Kopp law (the weighted average with fractions of constituents) over 890 K, the same as σ_e, due to the short-range order. Therefore, the disappearance point is expected to be above 890 K.

The liquid σ_e is obtained at several temperatures (750 K–900 K) using the K-G formula with snapshots of AIMD calculations (Fig. 14). The *ab initio* prediction, however, shows metallic behavior (decreasing with temperature) and higher values than the experiment. This is due to the assumption of the K-G formula, derived from the Kubo formula with the approximation of noninteracting Fermi system for the current operator [158]. It suggests that the K-G formula is suitable only for perfect crystal without inelastic processes, but the scattering between the electrons and the phonons always occurs in the semiconductor [158,159]. Also, the formula cannot directly describe zero σ_e for localized states [159]. Therefore, the result shows that the predicted σ_e is for ideal metallic behavior (NFE metal) without any consideration of remaining short-range interactions. Although there is a large discrepancy, the result can be used to assess the liquid σ_e for the Ag-added CdSb not reported so far (see next section).

The estimated $k(s)$ and $k(l)$ at T_{sl} are 2.0 and 9.9 W/m K, respectively, and lead to $Z_{TCS} = 4.0$. The high thermal conductivity jump is achieved by the transition from solid semiconductor to liquid metal (metallic melting). Also, the electron-poor characteristic yields high Z_{TCS} by lowering the k_p contribution. Therefore, CdSb is one of the notable TCS materials. Furthermore, the Z_{TCS} can be enhanced by suppressing k_{e+h} by adding Ag. We will discuss the transport characteristics of Ag-added CdSb in the next section.

D. Effect of Ag addition on CdSb

The point-defect (impurity) scattering is considered to predict k_p for Ag-added CdSb. The impurity in the base material, called static imperfection [1], hinders phonon transport, thus lowers k_p. The effect of point-defect scattering is found using the relation $1/k_p(x) = 1/k_p(0) + 1/k_{p,\mathrm{d}}$ [160], and $k_{p,\mathrm{d}}$ is found from [161,162]

$$k_{p,\mathrm{d}} = \frac{k_\mathrm{B}}{4\pi u_{p,g,\mathrm{A}}(a_1 CT)^{1/2}}, \tag{17}$$

where $u_{p,g,\mathrm{A}}$ is the acoustic phonon group velocity, a_1 is coefficient for the Rayleigh point-defect scattering, and CT is relaxation time for interphonon scattering. These parameters can be written as [1,160–162]

$$\frac{1}{u_{p,g,\mathrm{A}}} = \frac{1}{3}\left(\frac{1}{u_{p,g,\mathrm{LA}}} + \frac{1}{u_{p,g,\mathrm{TA1}}} + \frac{1}{u_{p,g,\mathrm{TA2}}}\right), \tag{18}$$

$$a_1 = \frac{V_c \Gamma}{4\pi u_{p,g,\mathrm{A}}^3}, \tag{19}$$

$$\Gamma = \sum x(1-x)\left[\frac{M(X)}{M_c}\right]^2, \tag{20}$$

$$CT = \frac{(6n)^{1/3} k_\mathrm{B}}{2\pi^{4/3} k_p(0)}, \tag{21}$$

where LA and TA denote for the longitudinal and transverse acoustic, V_c is unit cell volume, Γ is mass fluctuation scattering parameter, x and $M(X)$ are fraction and mass of added atom X, and M_c is mass of an average cluster. It can be assumed that the average unit cell volume and phonon group velocities of materials with small content of impurity (small x) are almost the same as pure base material (negligible effect). For unit cell $Cd_{8-x}Sb_8Ag_x$, $M_c = (8-x)M(\mathrm{Cd}) + xM(\mathrm{Ag}) + 8M(\mathrm{Sb})$, where $M(\mathrm{Cd}) = 112.411$, $M(\mathrm{Ag}) = 107.868$, and $M(\mathrm{Sb}) = 121.760$ g/mol. Using $x = 0.008$ (0.1%), $u_{p,g,\mathrm{A}} = 1450$ m/s (for entire Brillouin zone) [94], and the Slack relation for pure CdSb to the $k_p(0)$, k_p for 0.1% Ag-added CdSb, is predicted in the Fig. 15. The calculated k_p is slightly lower than k_p for pure CdSb, 0.06 and 0.02 W/m K at 300 K and T_{sl} (about 5%), respectively. This shows that addition of Ag does not change k_p significantly. It is expected that the k_f is also lowered because the speed of sound will decrease, but the effect is minor. We assume k_f is the same as k_p at T_{sl}, which makes it lower than pure CdSb; this way Z_{TCS} is slightly underestimated.

The solid k_e (Fig. 15) of Ag-added CdSb is 0.8 W/m K at T_{sl} much higher than pure CdSb (0.2 W/m K); thus, the addition of an Ag atom exerts an effect to the solid-state electronic structure. The estimated $k(s) = k_p + k_e$ is almost the same to the experimental result [48] and suggests that k_{e+h} is significantly decreased. This is because of an increase in hole concentration, which leads to a decrease in Seebeck coefficient [48,73] and unbalanced σ_e between majority (hole) and minority (electron) carriers. So, although k_e increases, $k(s)$ decreases highly about 0.8 W/m K, due to the considerable decrease in the k_{e+h}. Therefore, Z_{TCS} can enhance noticeably, provided that the liquid σ_e is still as high as that of pure CdSb.

The liquid σ_e of Ag-added CdSb at 800 K is calculated by the K-G formula, with the same method used for pure CdSb. Two Cd atoms in the CdSb supercell are replaced with Ag atoms (3.1%) positioned as far as possible between them. Note that such a small addition is hard to be realized by *ab initio* calculations due to large system size. The result shows that the predicted σ_e at 800 K is 8074 $(\Omega\,\mathrm{cm})^{-1}$, almost the same as pure CdSb (8164 $(\Omega\,\mathrm{cm})^{-1}$), and should be the same for 0.1% Ag addition. Because the short-range order will not change with small content of Ag atom, the *ab initio* calculations suggest that the addition of Ag atom does not affect to the electron transport properties of liquid CdSb and k_e is the same as pure CdSb (9.4 W/m K at T_{sl}).

The estimated $k(s)$ and $k(l)$ at T_{sl} are 1.2 and 9.9 W/m K, respectively, and lead to $Z_{\mathrm{TCS}} = 7.3$ for the 0.1% Ag-added CdSb, significantly higher than that of pure CdSb (4.0) due to the k_{e+h} suppression. Therefore, the TCS performance of CdSb can be enhanced by the addition of an Ag atom.

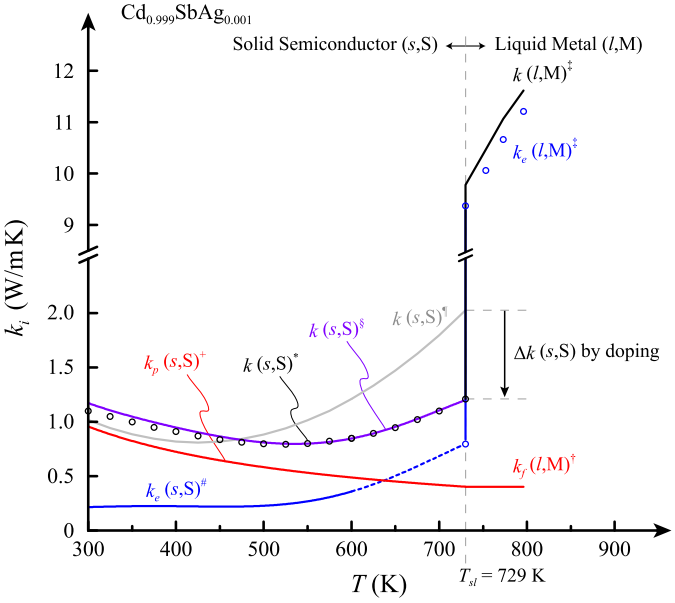

¶ Experimental result [48] for pure CdSb
* Experimental result [48] by measured properties ($k = \alpha\rho C_p$) up to 600 K, and extrapolated up to T_{sl}
# Experimental result [48] by W-F law using measured σ_e up to 600 K, and extrapolated up to T_{sl}
+ Predicted by the theoretical model (see text)
§ Calculated by $k = k_p(s,\mathrm{S}) + k_e(s,\mathrm{S})$
† Assumption; $k_f(l,\mathrm{M})$ the same as $k_p(s,\mathrm{S})$ at T_{sl}
‡ k_e the same as that of pure CdSb, and $k(l,\mathrm{M}) = k_f(l,\mathrm{M}) + k_e(l,\mathrm{M})$

FIG. 15. Temperature dependence of the thermal conductivities for the 0.1% Ag-added CdSb for the solid and liquid phase. The k_e is estimated from the measured σ_e, whereas the k_p is predicted by the Slack relation with the point-defect (impurity) scattering. The predicted and experimental (black circles) results for $k(s)$ are compared, along with those for pure CdSb. The liquid k_e is the same as that of pure CdSb, since the liquid σ_e predicted by the K-G treatment did not change by added Ag.

VII. HIGH Z_{TCS} Zn_3Sb_2

A. Lattice and transport properties of Zn_4Sb_3

Zn-Sb compounds (ZnSb, Zn_4Sb_3, and Zn_3Sb_2) are known as semiconductors [163] undergoing metallic melting [52], and the first two are thermoelectric (TE) materials for their low thermal conductivity [95,96,164–167]. Their liquid σ_e at T_{sl} is higher than Cd-Sb [52], so large Z_{TCS} is expected when $k(s)$ is low near T_{sl}. While ZnSb undergoes incongruent

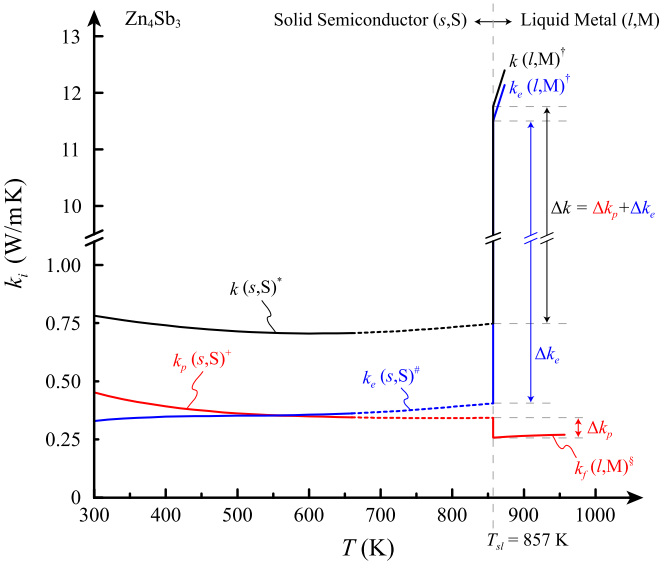

* Experimental result [172] by measured properties ($k = \alpha\rho C_p$) up to 660 K, and extrapolated up to T_{sl}
+ Experimental result [172] by $k\,(s,S) - k_e\,(s,S)$ up to 660 K, and extrapolated up to T_{sl}
# Experimental result [172] by W-F law using measured σ_e up to 660 K, and by $k\,(s,S) - k_p\,(s,S)$ up to T_{sl}
§ Calculated by Bridgman theory [1] using measured speed of sound and molar volume [104]
† k_e is Calculated by W-F law using suggested σ_e [52] and $k\,(l,M) = k_f\,(l,M) + k_e\,(l,M)$

FIG. 16. Temperature dependence of the thermal conductivities of β-Zn_4Sb_3 for the solid and liquid phase, assuming that the transport characteristic of β-Zn_4Sb_3 is the same as γ-Zn_4Sb_3. The k_p is rather very small, due to the interstitial Zn atoms which cause considerable phonon scattering. Also, the dependence of solid k_e on temperature make it small, resulting from solid σ_e decreasing with temperature increase (Fig. 17). However, the liquid k_e is larger than that of CdSb.

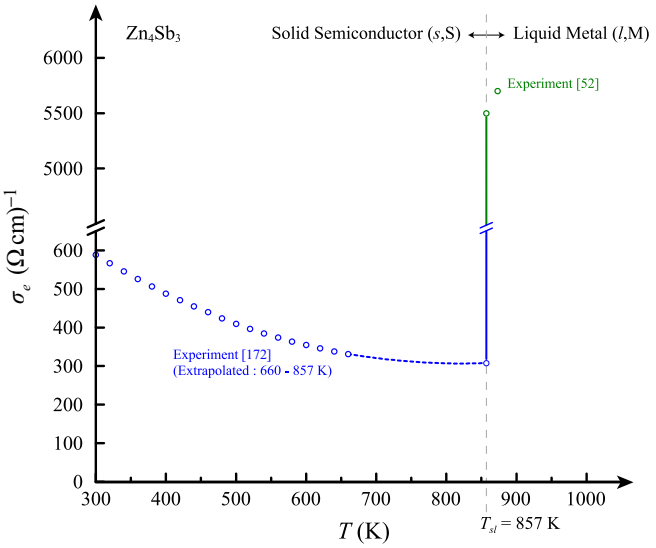

FIG. 17. Temperature dependence of σ_e of the solid and liquid β-Zn_4Sb_3, with significant rise (high Z_{TCS}) in the S/M transition at T_{sl}. The solid σ_e decreases with temperature because the mobility decreases considerably, and that of liquid increases with temperature as CdSb due to the short-range order interactions.

melting, Zn_3Sb_2 data is rare [92], but its Z_{TCS} is expected not to be smaller than the better-known Zn_4Sb_3. So we examine structure and transport characteristics of Zn_4Sb_3 comparing with Zn_3Sb_2. Zn_4Sb_3 has several solid phases (transitions between α/β and β/γ occur at 253 K and 763 K) and melts at 857 K [168]. We analyze yet better-known TE β-Zn_4Sb_3 with rather low thermal conductivity 0.75 W/m K over a wide temperature range (Fig. 16), unlike CdSb; i.e., k_{e+h} is negligible is due to the large band gap (1.0 eV [88]).

The low k_p of β-Zn_4Sb_3 is due to its complicated structure, which has uncertainty due to partial occupancy of Zn atoms, and the stoichiometry is not 4:3 but rather 3.95:3 [95]. The main structure is rhombohedral as $Zn_{36}Sb_{30}$ with the electron defficiency [91], and Sb atoms have full occupancy at each site but Zn1 atoms have 90% occupancy. There are three additional interstitial sites for Zn atoms (Zn2, Zn3, and Zn4) with partial occupancy of about 5% (36 available positions for each site). These interstitial Zn atoms make up for the electron-poor nature of main structure so that the charge balance is achieved [91]. Therefore, the partially occupied interstitial sites lead to significant point-defect scatterings [96]. Because of its soft and anharmonic bonding (loosely bound Zn atoms), the ionic conductivity is high and Zn atoms will move to vacancies easily (leading to less-ordered structure), and the Sb dumbbells (vertical Sb-Sb bonds) [169] cannot rattle independently [96,166]. Also, there are nanovoids or nanoparticles of Zn or ZnSb within the structure [96], causing significant phonon scattering.

Its solid k_e is also small over a wide range of temperature, since its σ_e decreases with temperature [93,96,170–172] (Fig. 17) due to the decay in electron mobility [96] compensating for increase in charge density. The acoustic phonon scattering is the source for the reduced mobility [96]. This can be associated with the partially occupied Zn atoms moving to vacancies more frequently as temperature increases and the atomic structure becomes much less ordered; thus, much active phonon-electron scattering as well as phonon-phonon scattering is expected as temperature increases. In addition, its smaller solid Lorenz number than metals or heavily doped semiconductors (1.86×10^{-8} W Ω/K^2 at 300 K) [172] leads to small solid k_e. Its liquid σ_e is about 5500 $(\Omega\,\text{cm})^{-1}$ [52] and k_e is 11.5 W/m K (higher than CdSb due to the higher σ_e and T_{sl}). The σ_e data (Fig. 17) and the previous reports [104,173] show that clusters of short-range order remain (same as CdSb), so liquid k_e increases with temperature (Fig. 16). Using the Bridgman model and data [104] on speed of sound and molar volume give $k_f = 0.26$ W/m K at T_{sl}, slightly lower than k_p at T_{sl} (0.34 W/m K).

These transport properties of β-Zn_4Sb_3 give high $Z_{TCS} = 14.7$, the highest identified yet for bulk, passive TCS, if the transport characteristics of γ phase are the same β phase and the structure is stable at T_{sl}. There is controversy about its congruent melting [88,168] and it can be due to its instability. The Zn atoms may sublimate decomposing into ZnSb and Zn before melting [165,168]. However, its high temperature was claimed recently [167]; some Zn-Sb bonds break over 425 K and β phase becomes mixture of Zn and ZnSb, but it will become stable again over 565 K by reactions between ZnSb with Zn, when the structure of β phase is not decomposed too much between 425 K and 565 K.

We perform *ab initio* studies of the stability of β phase at high temperature to shed light. The structure has the space group of $R3c$ and the lattice constants are $a = b =$

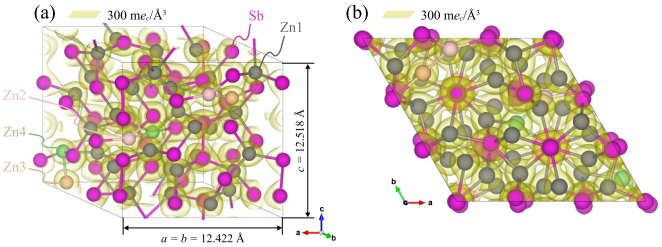

FIG. 18. *Ab initio* prediction of the β-Zn_4Sb_3 structure and its charge density distribution. The contours are for 300 $me_c/Å^3$. (a) Rhombohedral unit cell, where the vertical Sb-Sb bonds are dimers. (b) Top view of the structure. The Zn1 and Sb are atoms in the main structure, while Zn2, Zn3, and Zn4 are interstitial atoms. The predicted lattice constants and the bond lengths are in good agreement with available results (Table II).

12.228 Å and $c = 12.407$ Å [95]. The structure for the *ab initio* calculations is reconstructed by substituting three Zn1 atoms with six interstitial Zn atoms (two Zn atoms for each interstitial site) following recent study [174]. This $Zn_{39}Sb_{30}$ model possesses the occupancies for each Zn site (91.7% and 5.6% for main and interstitial sites, respectively), almost the same as those reported. The relaxed structure of β-Zn_4Sb_3 is presented in Fig. 18. Its lattice constants are $a = b = 12.422$ Å and $c = 12.518$ Å, almost the same as experiment [95], and and the bond lengths are similar to the previous *ab initio* calculation [174] (Table II). The bond length of interstitial Zn atoms is shorter than those of the main sites: 2.666–2.997 Å for Zn1-Sb, 2.659–2.935 Å for Zn1-Zn1, and 2.853–2.958 Å for Sb-Sb atoms. The measured length of Sb rattling dimers (six dumbbells in the unit cell) is 2.82 Å [95,168,169] and we have slightly longer dimer lengths 2.853–2.872 Å and 2.958 Å due to distortion by Zn3 and Zn4 atoms (differences are less than 2%), respectively. The AIMD is implemented for the relaxed unit cell structure at 700 K for 4 ps (Movie I [175]). The result shows that the Zn and Sb are not fixed at their prescribed positions; they wander inside the unit cell and the structure is not stable. So, we cannot observe stable β-phase lattice structure at high temperatures, and it would be possible that Zn_4Sb_3 melts incongruently.

B. Lattice and transport properties of Zn_3Sb_2

Although Zn_4Sb_3 may not be a TCS material due to the instability, its transport characteristics suggest the possibility of the highest Z_{TCS} from the Zn-Sb system, especially for the high-temperature stable Zn_3Sb_2 compound with congruent melting [91,104] at 853 K [62]. A recent report [97] regarding the structure of Zn_3Sb_2 suggests its TCS suitability. The structure is orthorhombic and has 6 atomic sites for Sb atoms and 18 for Zn atoms in the interstices made by Sb atoms (eight available positions for each site). The atomic sites for Sb atom have full occupancy, but the only one site for Zn has the full occupancy. Considering the partial occupancies for other Zn atoms, the actual composition of Zn_3Sb_2 is $Zn_{2.66}Sb_2 = Zn_4Sb_3$, almost the same as Zn_4Sb_3 ($Zn_{3.95}Sb_3$) but with slightly larger Zn content. There are 48 Sb in the unit cell of Zn_3Sb_2 and only 8 Zn are fully occupied, so there are additional 56 Zn (on average) at 136 possible positions in the unit cell. Thus, Zn_3Sb_2 has a significantly lower-ordered structure, more complicated and with a larger unit cell than β-Zn_4Sb_3. So, stronger anharmonicity, softer bonding, and higher ionic conductivity compared to Zn_4Sb_3 is expected with vigorous phonon-phonon and phonon-electron scatterings. Therefore, the k_p and solid σ_e would not be higher than those of β-Zn_4Sb_3. Also, considering the actual composition, it is evident that the liquid Zn_3Sb_2 and Zn_4Sb_3 have similar transport properties; i.e., Zn_3Sb_2 should have same $k(l)$ as Zn_4Sb_3. The previous report [52] identified Zn_3Sb_2 for liquid properties at 40% atomic fraction of Sb, but we believe that this is due to the lack of information for the structure and actual composition of Zn_3Sb_2 at that time. Therefore, it is expected that the Z_{TCS} of Zn_3Sb_2 is not smaller than Zn_4Sb_3 ($Z_{TCS} = 14.7$), and because of its stability it is anticipated that Zn_3Sb_2 is a promising TCS material.

TABLE II. Atomic structure properties of β-Zn_4Sb_3 predicted by *ab initio* calculations and compared with experiments [95] for lattice constants, and with previous *ab initio* results [174] for bond lengths.

Parameters	*Ab initio*	Previous reports	Error (%)
Lattice constants (Å)	$a = 12.422$	$a = 12.228$	1.59
	$c = 12.518$	$c = 12.407$	0.89
Bond length, Zn2-Zn3 (Å)	2.50	2.52	0.79
Bond length, Zn2-Zn4 (Å)	2.50	2.58	3.10
Bond length, Zn3-Zn4 (Å)	2.62	2.63	0.38

VIII. CONCLUSIONS

After a review of TCS materials, focusing on s/l phase change, we note that transition with nonelectronic transport (k_p and k_f) offers near-room-temperature T_{sl}, but not high Z_{TCS}; i.e., electronic transitions are preferred. Between M/M and S/M transitions, although M/M presents the highest Δk, S/M has the best potential for highest Z_{TCS}. The low k_p, absence of k_{e+h}, and large jump in k_e (i.e., σ_e) during the s/l, S/M transition are required to obtain high Z_{TCS}. While examining potential semiconductor compounds, we found that combinations of metal and semimetal/semiconductor elements are promising, especially with the semimetal elements (Sb and As) as the base elements. The binary antimonide and arsenide compounds with metal elements in group 12–15 are then investigated. The Sb is superior due to the higher σ_e of antimonides compared to arsenides (with the same metal element), and the Ag-added CdSb and possibly Zn_3Sb_2 have the highest Z_{TCS} (7.2 and 14.7, respectively).

Due to the electron-poor nature, the CdSb structure has nonuniform bond lengths and angles, and its three-center interaction (Cd-Sb-Cd) induces low phonon velocities and the strong anharmonicity, so the k_p of CdSb is low and its Z_{TCS} can be high. Using the charge density distribution and ELF, the electron local-/delocalization characteristics of the solid and liquid phases were demonstrated. In solid CdSb, the valence electrons are localized in the Cd-Sb and Sb-Sb covalent bonds, and one electron pair is shared in the three-center interaction, but the pair is more likely to be located on one side with

a shorter bond length. It is expected that the Cd atoms act as a metal in the liquid CdSb and contribute to its metallic properties, as in elemental liquid Cd. The ELF confirms that CdSb undergoes metallic melting and the retained short-range order interactions are for Cd_xSb_y clusters (the Sb-Sb cluster does not exist). Also, the D_e reveals that the main contribution to the band gap in the solid and in the metallic liquid is the $5p$ orbital of the Sb atoms.

The thermal conductivities in solid and liquid CdSb are obtained from existing experimental results and from theoretical and *ab initio* calculations. The Δk_e is the main contribution to the high thermal conductivity jump, and the k_{e+h} is estimated and distinguished from the k_p. It has been reported that the addition of Ag (0.1%) can significantly reduce k_{e+h}, and our *ab initio* calculations with the K-G formulation reveals that the liquid σ_e of Ag-added CdSb is the same as that of pure CdSb. Therefore, we confirmed that the Z_{TCS} can be notably enhanced by the Ag addition and becomes 7.2.

The Zn-Sb compounds have higher σ_e compared to the Cd-Sb system, and lower k_p. Specifically, β-Zn_4Sb_3 has a significantly low $k(s)$ of about 0.75 W/m K, due to the partial occupancy of the main and interstitial Zn atoms (which induce a very large unit cell, soft and anharmonic bonding, and active phonon scattering). However, Zn_4Sb_3 cannot be a TCS due to its structural instability at high temperatures and its incongruent melting. Although there are almost no data for the stable Zn_3Sb_2, it is expected that it has lower $k(s)$ compared to β-Zn_4Sb_3. The structure of Zn_3Sb_2 is more disordered than β-Zn_4Sb_3 since it has 17 Zn atom sites with partial occupancies and larger unit cell, so much more pronounced anharmonicity, softer bonds, and higher ionic conductivity are expected, so we expect its $k(s)$ will not be larger than that of β-Zn_4Sb_3 and should have Z_{TCS} higher than 14.7. We hope there will, in the future, be a detailed transport characterization of Zn_3Sb_2 as a distinct TCS material (and also as a high-temperature, high-Z_{TE} material).

ACKNOWLEDGMENTS

This work was supported by the NSF program on Thermal Transport and Processes (Award No. CBET1332807) and employed computing resources of the DOE National Energy Research Scientific Computing Center (Office of Science, Contract No. DE-AC02-05CH11231).

[1] M. Kaviany, *Heat Transfer Physics*, 2nd ed. (Cambridge University Press, New York, 2014).
[2] C. Kittel, *Introduction to Solid State Physics*, 8th ed. (Wiley & Sons, New York, 2005).
[3] A. F. May, E. S. Toberer, A. Saramat, and G. J. Snyder, Phys. Rev. B **80**, 125205 (2009).
[4] L. D. Zhao, H. J. Wu, S. Q. Hao, C. I. Wu, X. Y. Zhou, K. Biswas, J. Q. He, T. P. Hogan, C. Uher, C. Wolverton, V. P. Dravid, and M. G. Kanatzidis, Energy Environ. Sci. **6**, 3346 (2013).
[5] J. Yang, S. Wang, J. Yang, W. Zhang, and L. Chen, Mater. Res. Soc. Symp. Proc. **1490**, 9 (2013).
[6] G. Groetzinger, Nature (London) **135**, 1001 (1935).
[7] E. F. Steigmeier, Phys. Rev. **168**, 523 (1968).
[8] V. G. Gregorius, J. L. Chao, H. Toriumi, and R. A. Palmer, Chem. Phys. Lett. **179**, 491 (1991).
[9] M. Marinelli, F. Mercuri, U. Zammit, and F. Scudieri, Phys. Rev. E **58**, 5860 (1998).
[10] A. Fevrier and D. Morize, Cryogenics **13**, 603 (1973).
[11] H. Jin, O. D. Restrepo, N. Antolin, S. R. Boona, W. Windl, R. C. Myers, and J. P. Heremans, Nat. Mater. **14**, 601 (2015).
[12] S. Li, X. Ding, J. Ren, X. Moya, J. Li, J. Sun, and E. K. H. Salje, Sci. Rep. **4**, 6375 (2014).
[13] C. Dames, Nat. Nanotechnol. **7**, 82 (2012).
[14] J. Yang, Y. Yang, S. W. Waltermire, X. Wu, H. Zhang, T. Gutu, Y. Jiang, Y. Chen, A. A. Zinn, R. Prasher, T. T. Xu, and D. Li, Nat. Nanotechnol. **7**, 91 (2012).
[15] A. Shahriari and V. Bahadur, *ASME 2015 International Technical Conference and Exhibition on Packaging and Integration of Electronic and Photonic Microsystems collocated with the ASME 2015 13th International Conference on Nanochannels, Microchannels, and Minichannels* (ASME, 2015), Vol. 2, p. V002T06A007.
[16] M. A. Beasley, S. L. Firebaugh, R. L. Edwards, A. C. Keeney, and R. Osiander, Intersoc. Conf. Therm. Thermomech. Phenom. Electron. Syst, 9th **2**, 629 (2004).
[17] Y. Jia, G. Cha, and Y. S. Ju, Micromachines **3**, 10 (2012).
[18] Y. Jia and Y. S. Ju, J. Heat Transfer **136**, 074503 (2014).
[19] L. Duband, *Proceedings of the 15th International Cryocooler Conference in 2009* (ICC, Boulder, Co, 2009), p. 561.
[20] W. Hilberath and B. Vowinkel, Cryogenics **23**, 467 (1983).
[21] L. Stenmark, European Patent No. 1, 979,939 (15 October 2008).
[22] W. S. Williams, JOM **50**, 62 (1998).
[23] J. Bardeen, G. Rickayzen, and L. Tewordt, Phys. Rev. **113**, 982 (1959).
[24] C. W. Wang, D. Okawa, A. Majumdar, and A. Zettl, Science **314**, 1121 (2006).
[25] J. Zhu, K. Hippalgaonkar, S. Shen, K. Wang, Y. Abate, S. Lee, J. Wu, X. Yin, A. Majumdar, and X. Zhang, Nano Lett. **14**, 4867 (2014).
[26] Y. Li, X. Shen, Z. Wu, J. Huang, Y. Chen, Y. Ni, and J. Huang, Phys. Rev. Lett. **115**, 195503 (2015).
[27] R. F. Janninck and D. H. Whitmore, J. Phys. Chem. Solids **27**, 1183 (1966).
[28] A. O'Hara, T. N. Nunley, A. B. Posadas, S. Zollner, and A. A. Demkov, J. Appl. Phys. **116**, 213705 (2014).
[29] H. Kizuka, T. Yagi, J. Jia, Y. Yamashita, S. Nakamura, N. Taketoshi, and Y. Shigesato, Jpn. J. Appl. Phys. **54**, 053201 (2015).
[30] D.-W. Oh, C. Ko, S. Ramanathan, and D. G. Cahill, Appl. Phys. Lett. **96**, 151906 (2010).
[31] T. Zhang and T. Luo, ACS Nano **7**, 7592 (2013).
[32] C. Y. Ho, R. W. Powell, and P. E. Liley, J. Phys. Chem. Ref. Data **1**, 279 (1972).
[33] Ya. I. Dutchak, V. P. Osipenko, and P. V. Panasyuk, Izv. VUZov Fiz. **11**, 154 (1968).
[34] A. Y. Wu and R. J. Sladek, Phys. Rev. B **26**, 2159 (1982).
[35] H. Mehling and L. F. Cabeza, *Heat and Cold Storage with PCM* (Springer Science & Business Media, New York, 2008).

[36] G. B. Abdullaev, S. I. Mekhtieva, D. Sh. Abdinov, G. M. Aliev, and S. G. Alieva, Phys. Status Solidi B **13**, 315 (1966).

[37] A. K. Coker, *Ludwig's Applied Process Design for Chemical and Petrochemical Plants*, 4th ed. (Gulf Professional Publishing, New York, 2010), Vol. 2.

[38] V. A. Konstantinov, V. P. Revyakin, and V. V. Sagan, Low Temp. Phys. **37**, 420 (2011).

[39] G. J. Janz, C. B. Allen, N. P. Bansal, R. M. Murphy, and R. P. T. Tomkins, *Physical Properties Data Compilations Relevant to Energy Storage* (U. S. Department of Commerce, National Bureau of Standards, Washington, D.C., 1979), Vol. 2.

[40] R. Zheng, J. Gao, J. Wang, and G. Chen, Nat. Commun. **2**, 289 (2011).

[41] V. I. Fedorov and V. I. Machuev, Fiz. Tekh. Poluprovodn. **6**, 173 (1972) [Sov. Phys. Semicond. **6**, 142 (1972)].

[42] C. J. Glassbrenner and G. A. Slack, Phys. Rev. **134**, A1058 (1964).

[43] T. Nishi, H. Shibata, and H. Ohta, Mater. Trans. **44**, 2369 (2003).

[44] L. Crespi, A. Ghetti, M. Boniardi, and A. L. Lacaita, IEEE Electron Device Lett. **35**, 747 (2014).

[45] V. Ya. Prokhorenko, B. I. Sokolovskii, V. A. Alekseev, A. S. Basin, S. V. Stankus, and V. M. Sklyarchuk, Phys. Status Solidi B **113**, 453 (1982).

[46] S. Nakamura, T. Hibiya, and F. Yamamoto, J. Appl. Phys. **68**, 5125 (1990).

[47] E. Miller, J. Paces, and K. L. Komarek, Trans. Metall. Soc. AIME **230**, 1557 (1964).

[48] S. Wang, J. Yang, L. Wu, P. Wei, J. Yang, W. Zhang, and Y. Grin, Chem. Mater. **27**, 1071 (2015).

[49] E. F. Steigmeier and I. Kudman, Phys. Rev. **141**, 767 (1966).

[50] W. Nakwaski, J. Appl. Phys. **64**, 159 (1988).

[51] N. F. Mott and A. S. Alexandrov, *Sir Nevill Mott: 65 Years in Physics* (World Scientific, Singapore, 1995).

[52] A. Bath, J. G. Gasser, and R. Kleim, Phys. Lett. A **91**, 355 (1982).

[53] G. T. Dyos and T. Farrell, *Electrical Resistivity Handbook* (Peter Peregrinus, London, 1992).

[54] G. V. Samsonov, *Handbook of the Physicochemical Properties of the Elements* (Plenum, New York, 1968).

[55] R. W. Powell, M. J. Woodman, and R. P. Tye, Philos. Mag. **7**, 1183 (1962).

[56] M. V. Peralta-Martinez and W. A. Wakeham, Int. J. Thermophys. **22**, 395 (2001).

[57] C. L. Yaws, *Handbook of Thermal Conductivity* (Gulf Publishing, Houston, 1995), Vol. 4.

[58] X. Zhang, L. Shen, H. Wu, and S. Guo, Compos. Sci. Technol. **89**, 24 (2013).

[59] B. M. Mogilevskii, V. G. Surin, and A. F. Chudnovskii, J. Eng. Phys. Thermophys. **21**, 1297 (1971).

[60] V. A. Alekseev, A. A. Andreev, and M. V. Sadovskii, Sov. Phys. Uspekhi. Thermophys. **23**, 551 (1980).

[61] A. R. Regel, A. A. Andreev, B. A. Kotov, M. Mamadaliev, N. M. Okuneva, I. A. Smirnov, and E. V. Shadrichev, J. Non-Cryst. Solids **4**, 151 (1970).

[62] P. Villars, *Material Phases Data System (MPDS)* (Springer-Verlag, Heidelberg, Germany, 2014).

[63] J.-C. Tedenac, G. P. Vassilev, B. Daouchi, J. Rachidi, and G. Brun, Cryst. Res. Technol. **32**, 605 (1997).

[64] G. P. Vassilev, B. Daouchi, M.-C. Record, and J.-C. Tedenac, J. Alloys Compd. **269**, 107 (1998).

[65] S. Adachi, J. Appl. Phys. **53**, 8775 (1982).

[66] F. A. Lindemann, Z. Phys. **11**, 609 (1910).

[67] G. Grimvall and S. Sjodin, Phys. Scr. **10**, 340 (1974).

[68] B. R. Nag, J. Electron. Mater. **26**, 70 (1997).

[69] R. W. Keyes, Phys. Rev. **115**, 564 (1959).

[70] Ö. C. Yelgel and G. P. Srivastava, Phys. Rev. B **85**, 125207 (2012).

[71] Y. Lan, B. Poudel, Y. Ma, D. Wang, M. S. Dresselhaus, G. Chen, and Z. Ren, Nano Lett. **9**, 1419 (2009).

[72] H. Wu, J. Carrete, Z. Zhang, Y. Qu, X. Shen, Z. Wang, L.-D. Zhao, and J. He, NPG Asia Mater. **6**, e108 (2014).

[73] S. Wang, G. Zheng, T. Luo, X. She, H. Li, and X. Tang, J. Phys. D: Appl. Phys. **44**, 475304 (2011).

[74] H. J. Goldsmid and J. Sharp, Energies **8**, 6451 (2015).

[75] J.-H. Bahk and A. Shakouri, Appl. Phys. Lett. **105**, 052106 (2014).

[76] N. F. Mott, Rev. Mod. Phys. **40**, 677 (1968).

[77] T. G. Castner, N. K. Lee, G. S. Cieloszyk, and G. L. Salinger, Phys. Rev. Lett. **34**, 1627 (1975).

[78] N. F. Mott and E. A. Davis, Philos. Mag. **17**, 1269 (1968).

[79] F. Ermanis and E. Miller, J. Electrochem. Soc. **108**, 1048 (1961).

[80] H. Fritzsche and D. Adler, *Localization and Metal-Insulator Transitions* (Plenum, New York, 1985).

[81] L. Lindsay, D. A. Broido, and T. L. Reinecke, Phys. Rev. Lett. **111**, 025901 (2013).

[82] T. Okada, T. Satoh, M. Matsumura, and S. Ohno, J. Phys. Soc. Jpn. **65**, 230 (1995).

[83] T. Okada, T. Fujisawa, and S. Ohno, J. Non-Cryst. Solids **205-207**, 102 (1996).

[84] B. Predel and O. Madelung, *Landolt-Börnstein-Group IV Physical Chemistry* (Springer-Verlag, Berlin, 1991–1998), Vol. 5 A-J.

[85] C. Guminski, J. Phase Equilib. **17**, 419 (1996).

[86] K. Kovnir, Y. V. Kolen'ko, A. I. Baranov, I. S. Neira, A. V. Sobolev, M. Yoshimura, I. A. Presniakov, and A. V. Shevelkov, J. Solid State Chem. **182**, 630 (2009).

[87] H. M. Tütüncü and G. P. Srivastava, Solid State Commun. **221**, 24 (2015).

[88] O. Madelung, U. Rössler, and M. Schulz, *Landolt-Börnstein-Group III Condensed Matter* (Springer-Verlag, Berlin, 1998), Vol. 41C.

[89] D. P. Spitzer, G. A. Castellion, and G. Haacke, J. Appl. Phys. **37**, 3795 (1966).

[90] W. Klemm and H. Niermann, Angew. Chem. Int. Edit. **2**, 523 (1963).

[91] U. Häussermann and A. S. Mikhaylushkin, Dalton Trans. **39**, 1036 (2010).

[92] A. Fischer, D. Eklöf, D. E. Benson, Y. Wu, E.-W. Scheidt, W. Scherer, and U. Häussermann, Inorg. Chem. **53**, 8691 (2014).

[93] T. Caillat, J.-P. Fleurial, and A. Borshchevsky, J. Phys. Chem. Solids **58**, 1119 (1997).

[94] T. Pandey and A. K. Singh, Phys. Chem. Chem. Phys. **17**, 16917 (2015).

[95] G. J. Snyder, M. Christensen, E. Nishibori, T. Caillat, and B. B. Iversen, Nat. Mater. **3**, 458 (2004).

[96] E. S. Toberer, P. Rauwel, S. Gariel, J. Taftø, and G. J. Snyder, J. Mater. Chem. **20**, 9877 (2010).
[97] M. Boström and S. Lidin, J. Alloys Compd. **376**, 49 (2004).
[98] O. Madelung, U. Rössler, and M. Schulz, *Landolt-Börnstein-Group III Condensed Matter*, Vol. 41$A1\beta$ (Springer-Verlag, Berlin, 2002).
[99] H. N. G. Wadley and K. P. Dharmasena, J. Cryst. Growth **130**, 553 (1993).
[100] S. Adachi, *Properties of Group-IV, III-V and II-VI Semiconductors* (Wiley & Sons, West Sussex, U.K., 2005).
[101] V. Cháb, V. Šmíd, and L. Štourač, Czech. J. Phys. B **26**, 1059 (1976).
[102] R. Bowers, R. W. Ure, Jr., J. E. Bauerle, and A. J. Cornish, J. Appl. Phys. **30**, 930 (1959).
[103] Y. Tsuchiya, J. Phys. Soc. Jpn. **64**, 3547 (1995).
[104] Y. Tsuchiya and S. Kanai, J. Non-Cryst. Solids **156-158**, 433 (1993).
[105] G. Kresse and J. Furthmüller, Phys. Rev. B **54**, 11169 (1996).
[106] X. Gonze *et al.*, Comput. Phys. Commun. **180**, 2582 (2009).
[107] M. Torrent, F. Jollet, F. Bottin, G. Zerah, and X. Gonze, Comput. Mater. Sci. **42**, 337 (2008).
[108] J. P. Perdew, K. Burke, and M. Ernzerhof, Phys. Rev. Lett. **77**, 3865 (1996).
[109] P. E. Blöchl, Phys. Rev. B **50**, 17953 (1994).
[110] G. Kresse and D. Joubert, Phys. Rev. B **59**, 1758 (1999).
[111] S. Grimme, J. Antony, S. Ehrlich, and S. Krieg, J. Chem. Phys. **132**, 154104 (2010).
[112] S. Grimme, S. Ehrlich, and L. Goerigk, J. Comp. Chem. **32**, 1456 (2011).
[113] G. Kresse, M. Marsman, and J. Furthmüller, VASP the GUIDE (http://cms.mpi.univie.ac.at/vasp/vasp/vasp.html), 2015.
[114] J. Wang, G. Román-Pérez, J. M. Soler, E. Artacho, and M.-V. Fernández-Serra, J. Chem. Phys. **134**, 024516 (2011).
[115] A. D. Becke and E. R. Johnson, J. Chem. Phys. **124**, 221101 (2006).
[116] F. Tran and P. Blaha, Phys. Rev. Lett. **102**, 226401 (2009).
[117] H. Kim, M. H. Kim, and M. Kaviany, J. Appl. Phys. **115**, 123510 (2014).
[118] S. Yu and M. Kaviany, J. Chem. Phys. **140**, 064303 (2014).
[119] D. Li, P. Zhang, and J. Yan, Phys. Rev. B **84**, 184204 (2011).
[120] C. Woodward, M. Asta, D. R. Trinkle, J. Lill, and S. Angioletti-Uberti, J. Appl. Phys. **107**, 113522 (2010).
[121] V. Recoules and J.-P. Crocombette, Phys. Rev. B **72**, 104202 (2005).
[122] S. Mazevet, M. Torrent, V. Recoules, and F. Jollet, High. Energ. Dens. Phys. **6**, 84 (2010).
[123] R. Kubo, J. Phys. Soc. Jpn. **12**, 570 (1957).
[124] D. A. Greenwood, Proc. Phys. Soc. London **71**, 585 (1958).
[125] D. V. Knyazev and P. R. Levashov, Comput. Mater. Sci. **79**, 817 (2013).
[126] D. Houde, S. Jandl, and C. Carlone, J. Raman Spectrosc. **14**, 434 (1983).
[127] B. Cordero, V. Gómez, A. E. Platero-Prats, M. Revés, J. Echeverría, E. Cremades, F. Barragán, and S. Alvarez, Dalton Trans. **21**, 2832 (2008).
[128] A. A. Ashcheulov, O. N. Manik, and S. F. Marenkin, Inorg. Mater. **39**, S59 (2003).
[129] K.-J. Range, J. Pfauntsch, and U. Klement, Acta Crystallogr. C **44**, 2196 (1988).
[130] R. Kumar and C. S. Sivaramakrishnan, J. Mater. Sci. **6**, 48 (1971).
[131] J. E. Enderby and L. Walsh, Philos. Mag. **14**, 991 (1966).
[132] Y. Tsuchiya, J. Phys. Soc. Jpn. **64**, 159 (1995).
[133] A. A. Ashcheulov, O. N. Manyk, T. O. Manyk, S. F. Marenkin, and V. R. Bilynskiy-Slotylo, Inorg. Mater. **49**, 766 (2013).
[134] Y. Takagiwa and K. Kumura, Sci. Tech. Adv. Mater. **15**, 044802 (2014).
[135] B. Silvi and A. Savin, Nature (London) **371**, 683 (1994).
[136] K. Chen and S. Kamran, Model. Numer. Simulat. Mater. Sci. **3**, 7 (2013).
[137] G. Kresse and J. Hafner, Phys. Rev. B **55**, 7539 (1997).
[138] F. Kelemen, A. Neda, D. Niculescu, and E. Cruceanu, Phys. Status Solidi B **21**, 557 (1967).
[139] M. C. Roufosse, Pressure Dependence of the Thermal Conductivity of Complex Dielectric Solids, *Proceedings of the Fourteenth International Conference on Thermal Conductivity* (Springer Science+Business Media, New York, 1976).
[140] O. Madelung, *Semiconductors: Data Handbook*, 3rd ed. (Springer-Verlag, Berlin, 2012).
[141] P. Price, Philos. Mag. **46**, 1252 (1955).
[142] H. Goldsmid, Proc. Phys. Soc. Sec. B **69**, 203 (1956).
[143] S. Wang, J. Yang, T. Toll, J. yang, W. Zhang, and X. Tang, Sci. Rep. **5**, 10136 (2015).
[144] G. A. Slack and M. A. Hussain, J. Appl. Phys. **70**, 2694 (1991).
[145] H. J. Goldsmid and J. W. Sharp, J. Electron. Mater. **28**, 869 (1999).
[146] N. Dahbi, M. Daoudi, and A. Belghachi, Int. J. Math., Comput., Phys., Electrical Comput. Eng. **5**, 950 (2011).
[147] Y.-L. Pei, J. He, J.-F. Li, F. Li, Q. Liu, W. Pan, C. Barreteau, D. Berardan, N. Dragoe, and L.-D. Zhao, NPG Asia Mater. **5**, e47 (2013).
[148] Y. Yamada, J. Phys. Soc. Jpn. **35**, 1600 (1973).
[149] A. Hrubý, I. Kubelík, and L. Štourač, Czech. J. Phys. B **15**, 740 (1965).
[150] A. Lashkul, Quantum transport phenomena and shallow impurity states in CdSb, Ph.D. thesis, Lappeenranta University of Technology, Lappeenranta, 2007.
[151] I. M. Pilat, in *Proceedings of the 4th All-Union Conference on Semiconductor Materials*, edited by N. Kh. Abrikosov (Consultants Bureau Enterprises Inc., New York, 1963), p. 66.
[152] G. V. Rakin, Izv. VUZov. Fiz. **6**, 28 (1966).
[153] I. J. McColm, *Dictionary of Ceramic Science and Engineering*, 2nd ed. (Springer Science+Business Media, New York, 1994).
[154] I. K. Andronik and M. V. Kot, Bull. Russ. Acad. Sci. Phys. **28**, 929 (1964).
[155] W. J. Turner, A. S. Fischler, and W. E. Reese, Phys. Rev. **121**, 759 (1961).
[156] B. Predel, M. Hoch, and M. Pool, *Phase Diagrams and Heterogeneous Equilibria* (Springer-Verlag, Berlin, 2004).
[157] S. N. Chizhevskaya, Z. A. Danil'chenko, and V. L. Kurbatov, Izv. Akad. Nauk SSSR, Neorg. Mater. **10**, 1397 (1974).
[158] P. B. Allen, *Contemporary Concepts of Condensed Matter Science* (Elsevier, Amsterdam, 2006), Vol. 2, Chap. 6.
[159] P. Boolchand, *Insulating and Semiconducting Glasses*, Series on Directions in Condensed Matter Physics Vol. 17 (World Scientific, Singapore, 2000).

[160] H. Kim, M. Kaviany, J. C. Thomas, A. Van der Ven, C. Uher, and B. Huang, Phys. Rev. Lett. **105**, 265901 (2010).
[161] P. G. Klemens, Phys. Rev. **119**, 507 (1960).
[162] J. Callaway and H. C. von Baeyer, Phys. Rev. **120**, 1149 (1960).
[163] J. Burgess and R. H. Prince, *Zinc: Inorganic & Coordination Chemistry*, Encyclopedia of Inorganic and Bioinorganic Chemistry (Wiley & Sons, West Sussex, U.K., 2011).
[164] Y. Wu, J. Nylén, C. Naseyowma, N. Newman, F. J. Garcia-Garcia, and U. Häussermann, Chem. Mater. **21**, 151 (2009).
[165] D-B. Xiong, N. L. Okamoto, and H. Inui, Scr. Mater. **69**, 397 (2013).
[166] L. Bjerg, B. B. Iversen, and G. K. H. Madsen, Phys. Rev. B **89**, 024304 (2014).
[167] J. Lin, X. Li, G. Qiao, Z. Wang, J. Carrete, Y. Ren, L. Ma, Y. Fei, B. Yang, L. Lei, and J. Li, J. Am. Chem. Soc. **136**, 1497 (2014).
[168] Y. Mozharivskyj, A. O. Pecharsky, S. Bud'ko, and G. J. Miller, Chem. Mater. **16**, 1580 (2004).
[169] W. Schweika, R. P. Hermann, M. Prager, J. Perßon, and V. Keppens, Phys. Rev. Lett. **99**, 125501 (2007).
[170] M. Tsutsui, L. T. Zhang, K. Ito, and M. Yamaguchi, Intermetallics **12**, 809 (2004).
[171] M. Chitroub, F. Besse, and H. Scherrer, J. Alloys Compd. **460**, 90 (2008).
[172] S. Y. Wang, X. Y. She, G. Zheng, F. Fu, H. Li, and X. F. Tang, J. Electron. Mater. **41**, 1091 (2012).
[173] A. Sinha and E. Miller, Metall. Mater. Trans. B **1**, 1365 (1970).
[174] A. N. Qiu, L. T. Zhang, and J. S. Wu, Phys. Rev. B **81**, 035203 (2010).
[175] See Supplemental Material at http://link.aps.org/supplemental/10.1103/PhysRevB.94.155203 for the *ab initio* molecular dynamics calculation for β-Zn_4Sb_3 lattice structure at 700 K for 4 ps.